



A study of ensemble-sensitivity-based initial condition perturbation methods for convection-permitting ensemble forecasts

Xinyan Zhang, Jinzhong Min*, Tianjie Wu

Key Laboratory of Meteorological Disaster of Ministry of Education (KLME)/Joint International Research Laboratory of Climate and Environment Change (ILCEC)/ Collaborative Innovation Center on Forecast and Evaluation of Meteorological Disasters (CIC-FEMD), Nanjing University of Information Science & Technology, Nanjing 210044, China

ARTICLE INFO

Keywords:

Ensemble-based sensitivity analysis
Initial condition perturbations
Convection-permitting ensemble forecasts

ABSTRACT

A sensitivity-based initial condition (IC) perturbation method for convection-permitting ensemble forecasts (CPEFs) is presented and preliminarily tested. The distribution of the perturbations is based on the sensitivity patterns from the ensemble sensitivity analysis (ESA) and the fast-growing perturbations calculated by the breeding growth mode (BGM). Two convective precipitation cases are used to quantitatively and qualitatively evaluate the impacts of the perturbation schemes on the ensemble forecast skill based on the Weather Research and Forecasting (WRF) model. To generate the sensitivity-based IC perturbations, ESA is applied to the short-term convective precipitation cases to calculate the sensitivity patterns. The analysis reveals the influential factors related to the evolution of weather situations that impact the strength of the forecast precipitation. The sensitivity patterns are introduced to the IC perturbations by a sensitivity-based BGM (SeBGM) method proposed in this research, and the response of the forecast skill to different perturbation magnitudes is examined. Ensemble forecasts with sensitivity-based IC perturbations can adapt to changes in the weather regime and provide accurate simulations of the placement and strength of convective systems, leading to improvements in the precipitation forecast skill.

1. Introduction

Due to increased computing power, numerical models are able to achieve a convective-aware level to explicitly forecast convective storms (Kain et al., 2006; Rotach et al., 2009; Seity et al., 2011; Kain et al., 2013; Bauer et al., 2015). Despite the added value provided by the convection-permitting forecasts (CPF), current CPFs still suffer from persistent problems. The limitations include the inaccurate representation of partially resolved processes, referred to as the gray zone (Shutts and Pallares, 2014; Berner et al., 2017; Gao et al., 2017), and the rapid upscale growth of small scale error (Lorenz, 1969; Hohenegger and Schär, 2007). To address these issues, the convection-permitting ensemble forecasts (CPEFs) (Zhang and Pu, 2010; Gebhardt et al., 2011; Schwartz et al., 2015; Clark et al., 2016) are designed to consider various uncertainties in prediction, such as the growth of initial condition (IC) errors (Peralta et al., 2012; Mulena et al., 2016; Bouttier et al., 2016), their evolution as a function of the atmospheric state (Lorenz, 1969; Ancell, 2013; Surcel et al., 2016), and the uncertainties from the numerical models (Christensen et al., 2015; Berner et al., 2015). As the impact of these uncertainties on forecasts varies

greatly in different cases (Surcel et al., 2016, 2017), the nature of the uncertainty in the ICs and its evolution, especially the effect of pre-convective environment on the subsequent convection forecasts, is an important area of research.

Sensitivity analysis (SA) is an effective methodology for investigating forecast uncertainties. According to previous studies, convection initiation and development are very sensitive to the mesoscale environment in the early period, such as local humidity, vertical wind shear, and instability (Weisman and Rotunno, 2000; Takemi, 2007; Weisman et al., 2008; Schumacher et al., 2013; Trier et al., 2017). The evolution of the mesoscale phenomena is usually controlled by the larger-scale environment, such as low-level jets and troughs (Garcia-Ortega et al., 2009; Duda and Gallus, 2013). Because of the inherently multiscale interaction affecting the forecasts of convective systems, SA studies are necessary for a better understanding of the relationship between the pre-convective environment uncertainties and convection forecasts. Numerous SA studies have been performed by various technologies, including initial perturbations (Martin and Xue, 2006; Melhauser and Zhang, 2012) and adjoint sensitivity methods (Errico and Vukicevic, 1992; Errico et al., 2016). As highlighted in these

* Corresponding author.

E-mail address: minjz@nuist.edu.cn (J. Min).

studies, the forecasts show significant sensitivity to the IC uncertainty and its evolution within numerical models. However, the traditional sensitivity analysis methods have various limitations like expensive computational efforts, certain subjectivity in analysis and inherent linear assumption. To account for the IC uncertainty in convection forecasts comprehensively, a SA technique that efficiently reveal the dynamic link of the forecasts and IC error growth is needed.

In recent years, ensemble-based sensitivity analysis (ESA) has been employed in research to statistically assess forecast sensitivity to the evolution of the ICs (Ancell and Hakim, 2007; Torn and Hakim, 2008). This method evaluates the sensitivity of convection forecasts by applying linear statistics to a set of nonlinear trajectories of the model, providing an estimate of forecast sensitivity that intrinsically represents the dynamics of error growth. The appliance of the nonlinear ensemble prediction in ESA method can overcome the limitation of linear assumption to a certain degree, enabling the sensitivity to provide meaningful information for understanding the nonlinear error growth in convection forecast (Bednarczyk and Ancell, 2015). To date, ESA has been increasingly applied to investigate the sensitivity of meso-small scale weather events, such as mesoscale vortices (Li et al., 2014), squall lines (Hanley et al., 2013), dryline convection (Bednarczyk and Ancell, 2015; Torn and Romine, 2015; Hill et al., 2016; Berman et al., 2017; Torn et al., 2017) and supercell storms (Yokota et al., 2016; Limpert and Houston, 2018). The research suggests that the multiscale interactive environment has an important and long-lasting impact on the later convection. The change in strength and position of the sensitive synoptic systems will modulate the mesoscale thermodynamic conditions, making the convection more intensive or weaker. As demonstrated by these studies, ESA has great potential to understand the mechanism of convective initiation and development. In addition, ESA has also shown promise in the design of observation networks (Xie et al., 2013; Hitchcock et al., 2016; Limpert and Houston, 2018), where the impact of the observation locations can be estimated.

Although many studies have successfully applied ESA to convection storms to address the sensitivity to the pre-convective environment, the research to the evaluation and application of ESA results in CPEFs are relatively limited (Wang and Tan, 2010; Wile et al., 2015; Ancell, 2016). Nevertheless, one appealing advantage of the ESA is that it can foresee the evolution tendency of the forecast metrics with the modification of weather situations. The revealed sensitivity relationship provides valuable indications to the forecasts, especially for the convection which is very sensitive to the small changes of meteorological conditions (Schumacher et al., 2013; Bednarczyk and Ancell, 2015; Hill et al., 2016; Greybush et al., 2017). Berman et al. (2017) and Torn et al. (2017) examined the forecast errors of the model state variables within the sensitive regions, showing that the members forecasting convection closer to reality have statistically smaller errors. Ancell (2016) chose ensemble subsets with smallest error in regions with large ensemble sensitivity to improve subsequent forecast. Therefore the areas with higher sensitivity values can be more critical for subsequent forecasts if the sensitivity estimates from ESA are robust and meaningful. The sensitivity information, which can be conveniently obtained from the historical ensemble forecasts data, has the potential to provide guidance for the forecast of future weather.

Based on previous research, this study aims to: a) build sensitivity-based IC perturbations for CPEFs, where the nature of sensitivity patterns over time is considered; b) prove the hypothesis that the sensitivity factors revealed by ESA are significant for subsequent predictions. To meet the goal of this study, several ensemble experiments are designed for a better understanding of forecast uncertainty due to errors in the pre-convective environment. The feasibility of the method is theoretically proved by the experiment, but different settings would be required for practical application. we introduce the normalized sensitivity patterns from ESA to modulate the perturbation structure based on the operational IC perturbation techniques, and evaluate the response of the forecasts. In this way the perturbation at the sensitive area

is amplified without changing the overall magnitude of the perturbation field. Among the various methods for generating IC perturbations, the breeding growth mode (BGM) method (Toth and Kalnay, 1993, 1997) is applied due to its advantage of capturing the persistently growing perturbation associated with the evolving atmospheric flow via a simple procedure. This research introduces a concept that combines ESA and the BGM method, namely, sensitivity-based BGM (hereafter SeBGM). The SeBGM method aims to enhance the contribution of the fast-growing perturbation structure while promoting the development of the perturbation in highly sensitive regions. The perturbation fields are led to evolving in a direction that is more conducive to the forecast.

The rest of this paper is organized as follows. A brief overview of ESA and the introduction of SeBGM are presented in Section 2. Section 3 provides an overview of the cases and describes the details of the model implementation and experimental setup. Section 4 evaluates the results of ESA and the ensemble forecasts with the SeBGM method. The conclusion and discussion follow in Section 5.

2. Methodology

According to ESA method (Ancell and Hakim, 2007; Torn and Hakim, 2008), the sensitivity pattern (\mathbf{sp}) of a chosen forecast metric \mathbf{J} to a model state variable at earlier time \mathbf{x}_i is evaluated from an M -member ensemble ($i = 1, \dots, M$) via Eq. (1):

$$\mathbf{sp}_i = \frac{\partial \mathbf{J}}{\partial \mathbf{x}_i} = \frac{\text{cov}(\mathbf{J}, \mathbf{x}_i)}{\text{var}(\mathbf{x}_i)} \quad (1)$$

Where \mathbf{J} and \mathbf{x}_i are the $1 \times M$ ensemble estimates of the respective quantities. i is the state variable index. Cov denotes the covariance, and var. is the variance. The sensitivity value is equal to the slope of the line of the best fit for a linear regression between the ensemble estimates and the model state variable, which represents the expected change in response metric \mathbf{J} with a change in state variable \mathbf{x}_i . When calculating the sensitivity, the values of \mathbf{x}_i and \mathbf{J} are normalized by the ensemble standard deviation to eliminate the impact of the units, magnitudes and variances in different variables. By calculating the ensemble-based sensitivity of the forecast metric at different times, the resulting sensitivity patterns will update with changes in weather conditions, not only identifying sensitive regions that are crucial to the development of convection but also indicating the evolution of the initial error over time.

The BGM method generates perturbation fields that are determined by the error growth related to the development of atmospheric flow through the repeated dynamical cycle. It can be achieved via a simple procedure according to Toth and Kalnay (1993):

- a) Adding small arbitrary perturbations to the initial states at a given time t_0 .
- b) Integrating the model from the perturbed and unperturbed initial conditions for a time period (t_0-t_1) .
- c) Rescaling the difference fields between the perturbed forecasts and unperturbed forecasts to the same norm (root-mean-square amplitude or rotational kinetic energy) of the initial perturbation, and adding the rescaled difference fields to the analysis fields at the corresponding time.
- d) Repeating processes (b)–(c) forward in time to generate the final perturbation fields.

To combine the fast-growing perturbation from the BGM scheme and sensitivity patterns from the ESA into the final perturbation fields, the sensitivity-based BGM (SeBGM) method is proposed in this paper. The distribution of the perturbations is determined by both the dynamic growth in the breeding cycle and the sensitivity information in ESA. The perturbations are aimed at the crucial regions with high sensitivity and fast-growing error. In SeBGM method, the third step of the BGM procedure described above is modified to facilitate the introduction of

the sensitivity patterns. The sensitivity pattern is implemented as a product of the standardized sensitivity field and the difference between the perturbed forecasts \mathbf{x}_i^f and the unperturbed control forecasts \mathbf{x}_i^c . That is:

$$\alpha_i = \beta \cdot \mathbf{sp}_i \cdot (\mathbf{x}_i^f - \mathbf{x}_i^c) \quad (2)$$

Consistent with the Eq. (1), i is the variable index. \mathbf{sp}_i is the sensitivity matrix obtained by ESA, β is the rescaling factor determining the magnitudes of the perturbations. The analysis variable of the IC for the next breeding period \mathbf{x}_i^a is updated via the Eq. (3):

$$\mathbf{x}_i^s = (1 + \alpha_i) \mathbf{x}_i^a \quad (3)$$

where the \mathbf{x}_i^s is the updated analysis variable matrix for the next breeding cycle. The sensitivity patterns play the role of adjusting the spatiotemporal distribution of perturbations. The resulting perturbation fields vary with the update of the sensitivity pattern in each breeding cycle, which facilitates the perturbations to adapt consistently to the respective weather conditions. Since the introduction of the sensitivity patterns have modified the structure of the perturbation fields, instead of a fixed perturbation amplitude (i.e. the same norm as the initial perturbation) in the traditional BGM method (Toth and Kalnay, 1993, 1997; Hamill et al., 2000; Wang and Bishop, 2003; Deng et al., 2012), the parameter β is introduced and set to several different values to test the sensitivity of SeBGM scheme to the perturbation amplitudes.

3. Experimental design

3.1. Cases description

To determine whether the sensitivity-based IC perturbations can adapt to different geographic areas and weather situations, the effectiveness of the SeBGM scheme is examined via simulations of two case studies with different meteorological conditions. Case 1 is associated with a squall line in North China on 31 July 2013 (hereafter case0731), which caused strong convective precipitation in Beijing (black box in Fig. 2a) that occurred during a short period of time. Case 2 is a Meiyu front rainstorm occurred in Anhui province (The location is shown in Fig. 2) on 5 July 2013 (hereafter case0705).

For each case, an analysis box is defined to perform ESA for the convection forecast (black box in Fig. 1). The analysis box is defined according to the main center of the accumulated precipitation in the convective events, and the evaluation of the precipitation forecast is performed in the same analysis box for consistency. The size of the analysis boxes (43×57 grid points of the inner model domain with the resolution of 3 km) is the same for each case. The summary of the simulated case and the corresponding experiment setup are shown in Table 1.

3.2. Model configuration

The two-way nested ensemble are generated based on version 3.8.1 of the Advanced Research version of the Weather Research and Forecasting (WRF) Model, with 15 km horizontal grid spacing in the outer domain and 3 km in the nested domain. The domain configuration for each case is shown in Fig. 2. Each domain has 35 vertical levels and a model top of 50 hPa. The initial and lateral boundary conditions are taken from the NCEP Global Forecast System Final Analysis (GFS-FNL) data. The parameterization schemes used in this experiment are the Thompson microphysics (Thompson et al., 2008), Rapid Radiative Transfer Model (RRTM) longwave radiation (Mlawer et al., 1997), Dudhia shortwave radiation (Dudhia, 1989), Yonsei University (YSU) boundary layer (Hong et al., 2006), Noah land-surface model (Ek, 2003), and Kain Fritsch cumulus (Kain, 2003). The cumulus parameterization is turned off for the nested domain.

Following the settings in previous ESA studies, the ICs of the

ensemble for sensitivity analysis and subsequent experiments are produced from a 50-member ensemble data assimilation system (Bednarczyk and Ancell, 2015; Torn and Romine, 2015; Berman et al., 2017). The ensembles are initialized at 0600UTC 28 July 2013 for case0731 and 0000UTC 2 July 2013 for case0705 (Table 1), with the random perturbations based on the NCEP background error covariance from WRF-3DVAR (Barker et al., 2012) added to the GFS-FNL fields interpolated to the model outer domain. The Data Assimilation Research Testbed (DART) (Anderson, 2009) ensemble adjustment Kalman filter (EAKF) (Anderson, 2001) system is applied to carry out the cycling assimilation for 2 days, the horizontal wind, temperature and moisture observations from radiosonde, surface marine reports, Aircraft Communications Addressing and Reporting System (ACARS), and surface land synoptic stations are assimilated. To maintain spread in the ensemble during the cycling phase, spatial and temporal variation of the adaptive covariance inflation (Anderson, 2001) and covariance localization are applied with an initial inflation of 1.02 and a standard deviation of 0.6. Inflation is also damped with a coefficient of 0.9. The outer domain is cycled every 6 h for a day then downscaled to the nested domain and the two domains are cycled for another 24 h before initializing the forecast.

3.3. Experimental setup

The performance of the SeBGM scheme is evaluated in ensemble forecast experiments in the case studies. The experiment is conducted with five procedures, that is: (1) Hindcasting experiment initialized by the 50-member EAKF analyses to simulate the pre-convective environment; (2) Calculating sensitivity of precipitation to model state variables from the hindcast results; (3) Introducing sensitivity patterns by breeding cycle with SeBGM scheme, and setting other experiments for comparison; (4) Ensemble forecasts of four different experiments; (5) A schematic overview of the implementation process of the experiment with SeBGM method in this study is depicted in Fig. 3. The corresponding time periods of each procedure ($t_i - t_n$) in the two cases are shown in Table 1. The four experiments compared in this study is summarized in Table 2. Each part of the experiment is described in detail below.

3.3.1. Hindcasting experiment

A 50-member ensemble used to simulate the pre-convection environment is initialized by the cycling WRF-DART EAKF data assimilation system described in last subsection. This configuration of ensemble assimilation system follows the settings in previous ESA studies (Bednarczyk and Ancell, 2015; Torn and Romine, 2015; Torn et al., 2017) to ensure that the sensitivity analysis results are sufficiently representative. Conducted before the initialization of the forecast, this simulation period is referred to as the hindcasting period, as shown in Table 1 and Fig. 3. The hindcasting experiment is used to represent the past atmospheric conditions, which is completed near analysis time of forecast experiments (1 h later than forecast experiments; Table 1).

3.3.2. Sensitivity analysis

The ESA is implemented on the results of the 50-member hindcast. The sensitivity of the response forecast metric to the state variables is calculated by Eq. (1) in Section 2. In this study, \mathbf{J} in Eq. (1) is the precipitation averaged in the analysis box (black box in Fig. 1) within $\pm 1h$ of forecast initialization, when precipitation in the analysis box begins to intensify in each case. The variables to be perturbed in subsequent forecast experiments are determined as the analysis state variables in ESA (\mathbf{x}_i in Eq. (1)), including the horizontal wind (u ; v), potential temperature (θ) and water vapor mixing ratio (qv). As shown in Fig. 3 and Table 1, the ESA is performed backward in intervals of 6 h based on the 50-member hindcast, and the sensitivity patterns of the precipitation to the variables (u , v , θ , qv) at four lead times (from 0 h to 18 h prior to the forecast initialization) are generated.

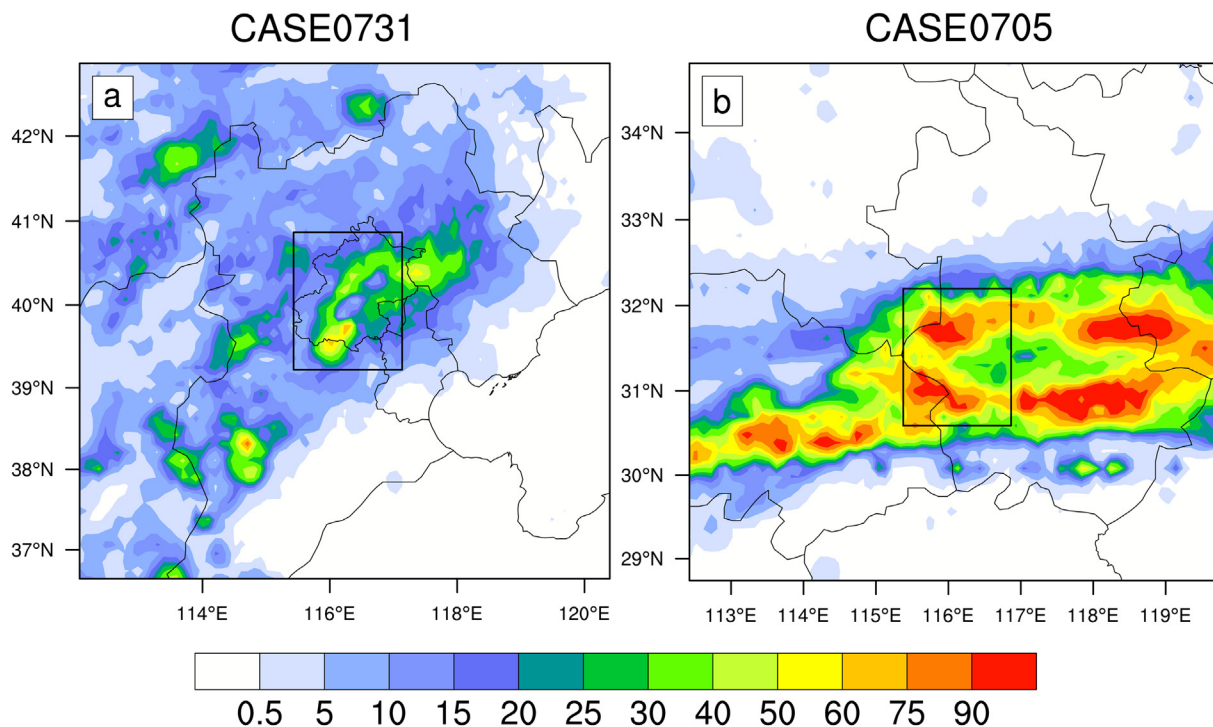


Fig. 1. The observed 12 h accumulated precipitation (mm) during (a) 0600-1800UTC 31 July for case0731 and (b) 0000-1200UTC 5 July for case0705. The black boxes denote the analysis areas for both cases.

3.3.3. Breeding

The obtained sensitivity patterns from ESA are introduced to the IC perturbations by breeding cycle with the SeBGM scheme. The breeding procedure is summarized in Section 2. Here we detail our settings for each item in the equations. The randomly selected 10 members of the 50-member EAKF analysis ICs are used as the initial ensemble analyses for breeding. The members are integrated forward to generate the perturbed forecasts x_i^f in Eq. (2) in Section 2. At the end of each cycle in breeding, the perturbations are calculated by the difference of the perturbed forecasts x_i^f and the control forecast x_i^c by Eq. (2). The sensitivity patterns are introduced as the sp matrix. The obtained sensitivity-based perturbations are added to the analysis variables x_i^a (u, v, θ, qv) by Eq. (3) with different magnitudes. To quantify the contribution of the introduced sensitivity patterns to subsequent forecasts intuitively, in this study we use the ensemble mean from the perturbed forecasts x_i^f as the analysis variable x_i^a in Eq. (3), such that no additional observation information is involved in the breeding cycle. The ICs of the forecast experiments are generated from a breeding period lasting 24 h (Table 1 and Fig. 3) with a 6 h cycle.

By modifying the β in Eq. (2), we define that the maximum value of the perturbation at each level is proportional to the standard deviation (STD) of the corresponding variable at this level. In this way, the variability of the variables at different times and vertical levels is considered in the perturbation. Eight ensemble experiments with perturbation magnitudes from 0.125 to 1 STD, defined as SENS_1–8, are designed to examine the forecast response to different perturbation amplitudes.

To further evaluate the contributions of the SeBGM scheme to the forecasting performance, two additional groups of experiments (GAUSS_1–8 and BGM_1–8) are conducted following the same procedures except for the introduction of the sensitivity patterns (sp in Eq. (2)). To determine whether the sensitivity patterns implemented here are reasonable and effective to achieve the systematic response in the model forecast, the GAUSS experiment is introduced, where the sp matrix in Eq. (2) is replaced by grid point-by-grid point Gaussian noise:

$$\alpha = \beta \cdot \text{gau} \cdot (x_i^f - x_i^c) \tag{4}$$

where the gau denotes the gaussian distribution with a mean of 0 and a STD of 1, so that the sensitivity patterns are compared with a random distribution. To assess what improvement the sensitivity-based perturbation yield compared to the raw fast-growing perturbation from the breeding method, the BGM experiment is performed, where the additional information added to perturbation is eliminated by setting sp to 1:

$$\alpha = \beta \cdot (x_i^f - x_i^c) \tag{5}$$

Like the SENS experiment, the β in the BGM and GAUSS experiments is also modified to eight different values.

3.3.4. Ensemble forecasts

As shown in Romine et al. (2013), the forecasts from the cycled ensemble assimilation analysis ICs still suffer from the systematic bias, and the improvements of the skill in convection-permitting forecasts only exist in short period (the first 12 h). The possible influence of the

Table 1

The cases in this study and the time setup in the experiments (the t_i-t_n is corresponding to the same annotations in Fig. 3).

Simulated cases	Case0731	Case0705
Data assimilation (t_r-t_0)	0600UTC 28 July–0600UTC 30 July	0000UTC 2 July–0000UTC 4 July
Hindcasting (t_0-t_5)	0600UTC 30 July–0700 UTC 31 July	0000UTC 4 July–0100UTC 5 July
Breeding(t_0-t_4)	0600UTC 30 July–0600UTC 31 July	0000UTC 4 July–0000UTC 5 July
Forecasting(t_4-t_n)	0600UTC–1800 UTC 31 July	0000UTC–1200UTC 5 July

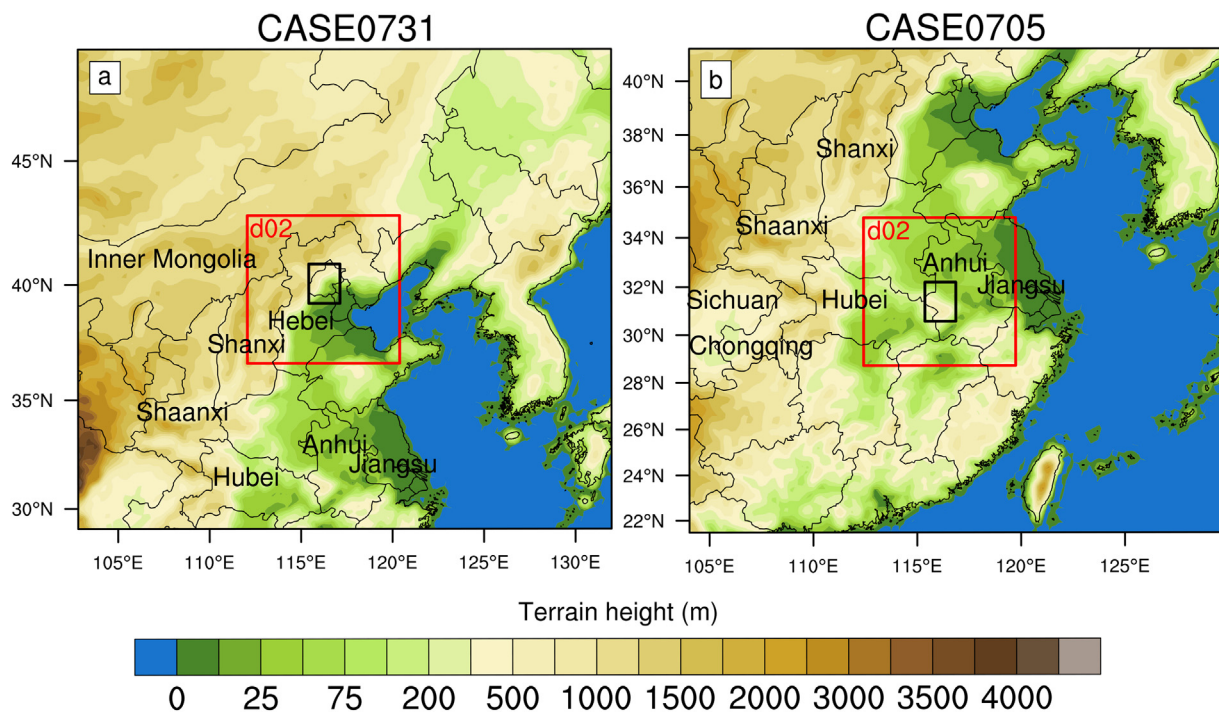


Fig. 2. Model domain configurations of case0731 (a) and case0705 (b). Red boxes denote the inner domain; black boxes are the analysis areas for both cases. The approximate locations of the provinces mentioned in Sections 3 and 4 are marked. (For interpretation of the references to colour in this figure legend, the reader is referred to the web version of this article.)

systematic bias and errors to the convection forecasts can also be represented in the ESA patterns, which offers helpful information to improve the subsequent forecasts. Therefore, the three groups of ensemble experiments (SENS, GAUSS and BGM) based on the breeding cycle are also compared with the forecasts initialized by original WRF-DART analysis. The forecasts initialized by the same selected 10 members of the 50-member WRF-DART EAKF analysis ICs are defined as the CONTROL ensemble experiment (Fig. 3).

The four groups of experiments are conducted and evaluated as shown in Table 2. For SENS, GAUSS and BGM experiments, the forecasts are initialized at the end of the last breeding cycle (The analysis

Table 2

The experimental set up in this study.

Experiment	Introduced pattern	10-member ensemble(s)	Breeding period	Integrating period
SENS	Sensitivity(sp)	8	24 h	12 h
GAUSS	Gaussian pattern(gau)	8	24 h	12 h
BGM	None	8	24 h	12 h
CONTROL	None	1	None	36 h

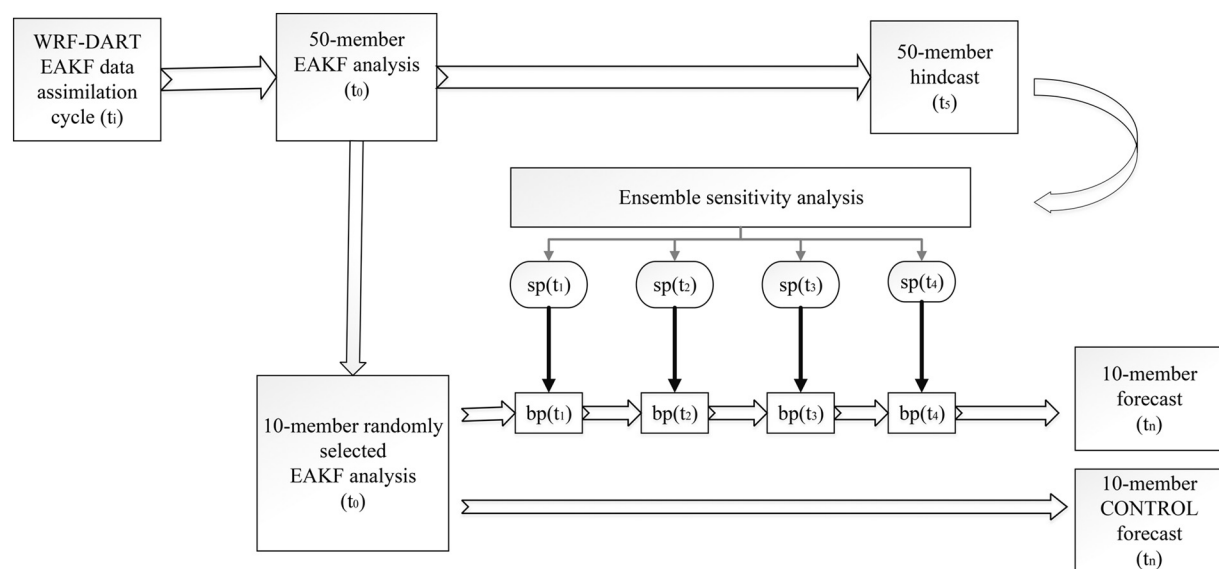


Fig. 3. Schematic representation of the experiment with SeBGM scheme and the CONTROL experiment for this study, where the *sp* denotes the sensitivity patterns introduced to the IC perturbations, the *bp* denotes the breeding period that produce the fast-growing perturbations by model dynamic cycle, all the swallowtail arrows indicate the model integration. The corresponding time periods t_i - t_n in each case are shown in Table 1.

time is t_4 in Fig. 3 and Table 1), and integrated forward for 12 h to forecast the short-term convective precipitation of the two cases. Each experiment has eight ensembles with perturbation magnitudes from 0.125 to 1 STD of the corresponding variables, defined as SENS_1–8, GAUSS_1–8, BGM_1–8 respectively, and each ensemble has 10 members. For CONTROL experiment, without the breeding period, one single ensemble with 10 members is initialized 24 h before and integrated forward for 36 h (The analysis time is t_0 in Fig. 3 and Table 1). In order to compare the four experiments in the same period, only the forecast during the 24–36 h lead times of CONTROL experiment is adopted in the evaluation. The comparison between CONTROL and SENS experiment aims to illustrate the benefit of sensitivity patterns to mitigate the forecast bias and errors in the later stage of CONTROL experiment.

3.4. Verification data and methods

Since the sensitivity analysis is performed for precipitation, the evaluation of the forecast results focuses on the impact of the SeBGM scheme on precipitation properties, and the non-precipitation variables are also considered. As described previously, the verification region of interest is defined as the same area as the forecast metric region of ESA (black box in Fig. 1), where the most intense precipitation is located.

3.4.1. Verification data

To assess the performance of the precipitation forecast, the hourly gridded precipitation data are derived from China’s automatic station and CMORPH fusion precipitation analyses datasets as the observation data in this study. The fusion precipitation analysis data is available at a spatial resolution of $0.1^\circ \times 0.1^\circ$ and in time intervals of 1 h and covering the area of $70^\circ - 140^\circ\text{E}$ and $15^\circ - 60^\circ\text{N}$ (Xie and Xiong, 2011).

The ERA5 reanalysis data from the European Centre for Medium-Range Weather Forecasts (ECWMF) applied in the verification of non-precipitation variables. The reanalysis data provides hourly analysis of a large number of atmospheric, land and oceanic climate variables, covering the Earth on a 30 km grid and atmospheric resolution with 137 levels from the surface up to a height of 80 km. The model outputs of the variables are interpolated bilinearly onto the space grids of the reanalysis data.

3.4.2. Verification method

The root-mean-square error (RMSE) of the ensemble mean accumulated precipitation, quantifying the distance between the forecast and the observation, is calculated first as a general measure of forecasting skill. Several skill scores are used to assess the performance of the precipitation forecasts. The forecast skill scores of the precipitation are calculated using the neighborhood ensemble probability (NEP) (Schwartz and Sobash, 2017), which is defined by averaging the ensemble probability (EP) at all points (N_r) over the radius (r) of influence:

$$NEP_{(i,j)} = \frac{1}{N_r} \sum_{k=1}^{N_r} EP_k \tag{6}$$

where the ensemble probability is calculated by averaging the binary probability (BP) of exceeding a specified precipitation rate threshold (q) within the ensemble members (N). That is:

$$EP_{(i,j)} = \frac{1}{N} \sum_{n=1}^N BP_{(i,j)} \tag{7}$$

$$BP_{(i,j)} = \begin{cases} 1, & f_{i,j} \geq q \\ 0, & f_{i,j} < q \end{cases} \tag{8}$$

While the skill scores generally increased with increasing influential radius, we identified a radius of 15 km to be appropriate for comparing

Table 3

The definition of miss, false alarm, hit and true negative.

Forecast\observed	Yes	No
$F_{(r)} > 0.5$	a(hit)	b(false alarm)
$F_{(r)} \leq 0.5$	c(miss)	d(true negative)

the performance in different experiments within a relatively small analysis box. The skill scores used here are briefly reviewed below:

The fraction skill scores (FSS) (Roberts and Lean, 2008; Zacharov and Rezacova, 2009) is calculated for different precipitation thresholds. First, the NEP of the model forecast and observations (denoted F and O) are calculated by Eqs. (6)–(8) ($N = 1$ for the observations in Eq. (7)), and the FSS for an influential radius r and domain size N_x by N_y grid points is defined based on Eq. (9):

$$FSS = 1 - \frac{\frac{1}{N_x N_y} \sum_{i=1}^{N_x} \sum_{j=1}^{N_y} [F_{(r)ij} - O_{(r)ij}]^2}{\frac{1}{N_x N_y} \left[\sum_{i=1}^{N_x} \sum_{j=1}^{N_y} F_{(r)ij}^2 + \sum_{i=1}^{N_x} \sum_{j=1}^{N_y} O_{(r)ij}^2 \right]} \tag{9}$$

The threat score (TS) is used to quantify the fraction of the correctly detected precipitation in the forecast. A contingency table is constructed by splitting the probabilities into two categories according to a decision threshold (Table 3). The TS can be computed via Eq. (10):

$$TS = \frac{a}{a + b + c} \tag{10}$$

To evaluate the different effects of the two noise patterns (sensitivity pattern and the Gaussian distribution) introduced to the perturbation, the Brier Skill Score (BSS), which is calculated using the NEP, is applied to assess the relative skill of the SENS and GAUSS experiments compared with that of the CONTROL experiments for each perturbation magnitude. The Brier Score is defined as:

$$BS_{(r)} = \frac{1}{N} \sum_{i=1}^N (F_{(r)i} - O_i)^2 \tag{11}$$

where O_i is 1 if the observed precipitation exceeds the specific threshold at i and is 0 otherwise. Then, the BSS is computed by Eq. (12):

$$BSS_{(r)} = 1 - \frac{BS_{(r)}}{BS_{(r),control}} \tag{12}$$

For the verification of the temperature, meridional wind and specific humidity, the temporally averaged RMSE of the ensemble mean and the ensemble spread in the analysis box are compared vertically at different pressure levels.

4. Results

4.1. ESA results

Before performing the sensitivity-based IC perturbations, the sensitivity patterns of the two cases from ESA are analyzed in this section. The previous research suggests that the significant sensitivity factors relate to the lower-tropospheric thermodynamic conditions (Torn and Romine, 2015; Berman et al., 2017; Torn et al., 2017), so that the sensitivity patterns of temperature and humidity for 800–900 hPa are detailed here to illustrate how the ESA represent the inherent relationship between the forecast and pre-convective environment.

4.1.1. case0731

The synoptic conditions on 30 July 2013 exhibit features favorable to the occurrence of convective outbreaks in North China (Fig. 4). The strong southwest wet flow is divided into two branches. The south branch transports abundant warm and moist air to the Jianghuai area ($30^\circ - 33^\circ\text{N}$, $115^\circ - 123^\circ\text{E}$, Anhui and Jiangsu area in Fig. 2), whereas the north branch south-west flow extends northeasterly to the North

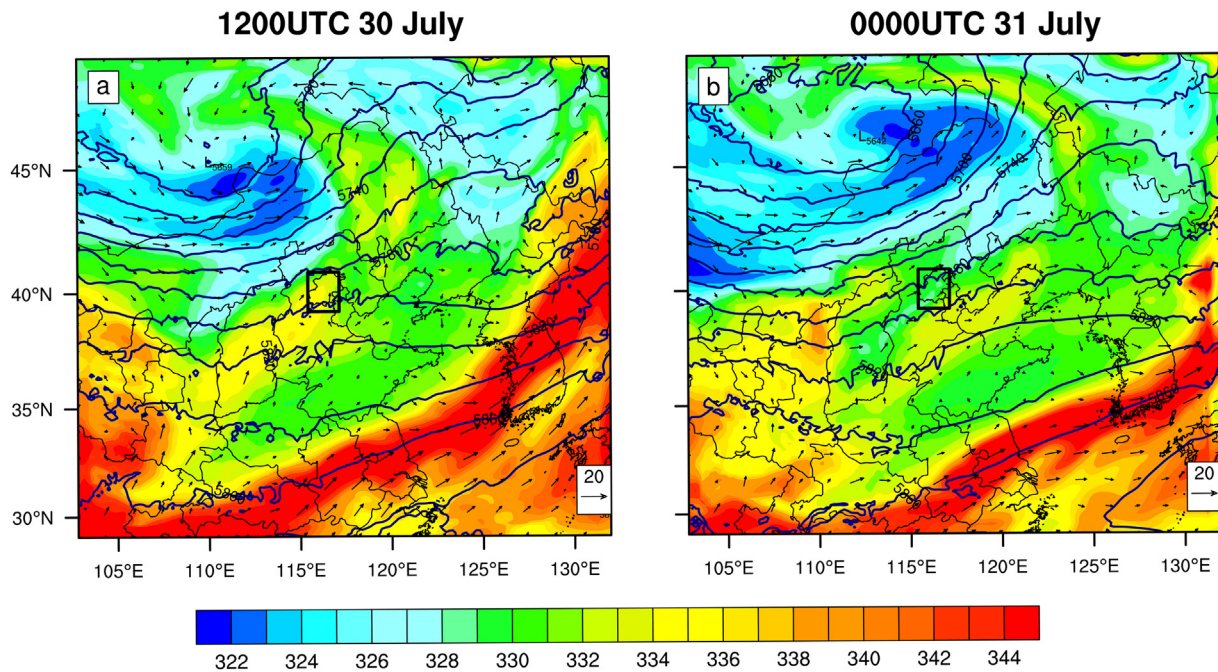


Fig. 4. WRF-DART analysis of equivalent potential temperature (θ_e , shading; k) and horizontal winds (vector; $m \cdot s^{-1}$) at 850 hPa and heights at 500 hPa (contours; m) for case0731, valid at (a) 18 h (1200UTC 30 July) and (b) 6 h (0000UTC 31 July) prior to the forecast initialized at 0600UTC 31 July. Black boxes denote the analysis area of ESA.

China region. A stable low-level cyclone over the Mongolian Plateau brings cold and dry air, and this event occurs in front of the deep trough, where the warm advection and the water vapor transportation are located. There is a significant gradient in θ_e through Inner Mongolia and Hebei province (40°N, 115°E; Fig. 2).

As shown in Fig. 5a, in the early stage (18 h prior to the forecast), the negative sensitivity of precipitation to q_v is maximized over the Jianghuai area to the Korean Peninsula, the southern side of the strong southwest wet flow, while the northern side is characterized by weak positive sensitivity. This sensitivity structure moves eastward over time to the south of the Korean peninsula (Fig. 5b), and the dipole signal becomes more obvious. It is suggested that increased water vapor on the northern side or decreased water vapor on the southern side of the southwest wet flow is associated with more precipitation. That is, more intensive precipitation occurs when the south branch of the southwest wet flow is farther to the north. A positive and negative symmetric sensitivity distribution appears along the southwest wet flow 6 h prior to the forecast (Fig. 5b). The region of the forecast metric (black box in Fig. 1) is near the axis of this symmetric distribution, indicating that moving the axis of the north branch of the southwest wet flow to the northwest is beneficial for increasing the precipitation in this region. Since the warm and wet air controlled by the southwest flow is moving southward, such a sensitivity distribution reflects a tendency of slower movement of the southwest flow, which contributes to the supply and maintenance of water vapor in Beijing. For this reason, the negative sensitivity on the south side of the system is usually relatively stronger. Meanwhile, the sensitivity pattern also exhibits a symmetric structure near the trough over the Mongolian region, with negative sensitivity at the back of the trough and positive sensitivity at the front, indicating that the eastward movement of the trough increases the precipitation.

The sensitivity to the potential temperature shows a north-south reverse distribution near the analysis area (Fig. 5c, d). Along the north branch of the southwest wet flow, a region of scattered but extensive negative sensitivity to the potential temperature is located over the southern portion of the domain 18 h prior to the forecast and is accompanied by stable positive sensitivity to its north (Fig. 5c). The positive and negative sensitivities both move eastward, and the negative

sensitivity is significantly strengthened at 0000UTC 31 July, 6 h prior to the forecast (Fig. 5d). The analysis area is at the junction of the positive and negative sensitivity areas. These sensitivity patterns indicate that the precipitation will increase as the north side of the analysis region warms and the south side cools. To the south of the cold center near northwestern Mongolia is a region of negative sensitivity that extends towards the south with the strengthening of the cold center, indicating a contribution of the southward intrusion of cold air to precipitation in the analysis area.

4.1.2. case0705

The synoptic setup on 4 July 2013 shows typical weather regimes of the Meiyu front rainstorm (Fig. 6). The central and eastern coasts of East China are under the edge of a subtropical high, whereas a low-level southwest jet extends from East China to the south of the Yellow Sea. Jianghuai region is experiencing conditions of high temperatures and humidity. Low vortex and shear lines are located in the middle and lower reaches of the Yangtze River, and the Meiyu front pushes southward over time.

The precipitation during 2300UTC 4 July - 0100UTC 5 July within the analysis box is strongly sensitive to the water vapor mixing ratio in the upstream regions (Fig. 7a) west of the analysis box over Hubei province (30°N, 112°E; Fig. 2), where the positive sensitivity is maximized. As the analysis box is in the south edge of the Meiyu front at this moment, the strong upstream positive sensitivity represents the contribution of the southwest water vapor transport as well as the southward movement of the Meiyu Front to the precipitation. With the movement of the Meiyu front, the analysis box is at the center of the Meiyu front at 1800UTC 4 July (Fig. 6b). The Meiyu front is oriented in a more northeast-southwest direction, accompanied by the weakening and the eastward movement of the positive sensitive region (Fig. 7b). North of the positive sensitivity area is a region of scattered negative sensitivity at 0600UTC (Fig. 7a) over the north of Shaanxi and Shanxi provinces (35 – 37°N, 110 – 115°E; Fig. 2) that moves southwestwards during the next 12 h (Fig. 7b). The coupling of the positive and negative sensitivity may also be tied to the movements of the shear line and the Meiyu front, revealing that the southward movement of the shear line

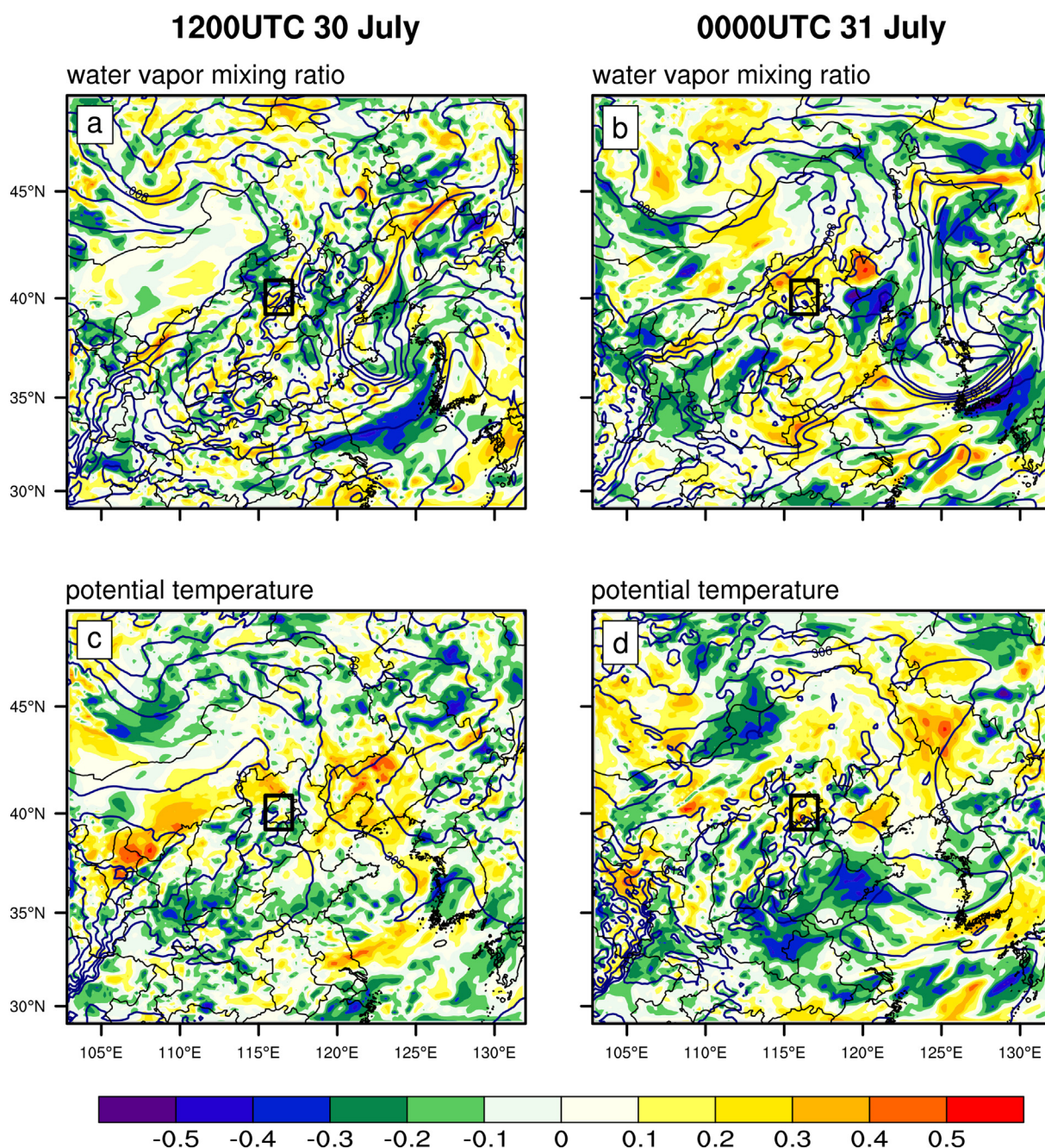


Fig. 5. Sensitivity of the spatially averaged precipitation during 0500-0700UTC 31 July averaged over the analysis area to the 800–900 hPa water vapor mixing ratio (q_v ; a, b) and the potential temperature (θ ; c, d) for case0731, valid at (a, c) 18 h (1200UTC 30 July) and (b, d) 6 h (0000UTC 31 July) prior to the forecast initialized at 0600UTC 31 July. The contours are the ensemble mean values for $q_v(kg \cdot kg^{-1})$, a, b) and potential temperature (K, c, d). Black boxes denote the analysis area of ESA.

and the Meiyu front contributes to the precipitation in the analysis box.

The sensitivity to temperature shows obvious coupled positive and negative distributions only near the west edge of the simulated domain over Chongqing and Sichuan provinces (30–32°N, 105–110°E; Fig. 2) 18 h prior to the forecast, suggesting a positive impact of the southward movement of warm air in this area on precipitation (Fig. 7c). Six hours prior to the forecast, a slender negative sensitivity line appears along the Yangtze River, and positive sensitivities are distributed on both sides of the negative line (Fig. 7d). How this distribution may directly impact the precipitation response remains unclear, but it may be tied to the Meiyu front. The following perturbation experiments may provide a clearer understanding of the impact of these sensitive regions on the precipitation forecast from another perspective.

4.2. Forecast verification

The sensitivity patterns are introduced to the IC perturbations by the SeBGM method described in Section 2 and the procedures discussed in Section 3.3. The forecast results of ensembles with different perturbation schemes (SENS, GAUSS, BGM and CONTROL) are estimated in the following subsection. The verification of the forecast result is performed first for precipitation, and non-precipitation variables such as temperature, specific humidity and horizontal winds are then considered in the verification to assess the performance of the ensembles more comprehensively.

The RMSE of the ensemble mean 12 h accumulated precipitation with respect to observation data in the analysis box are calculated for

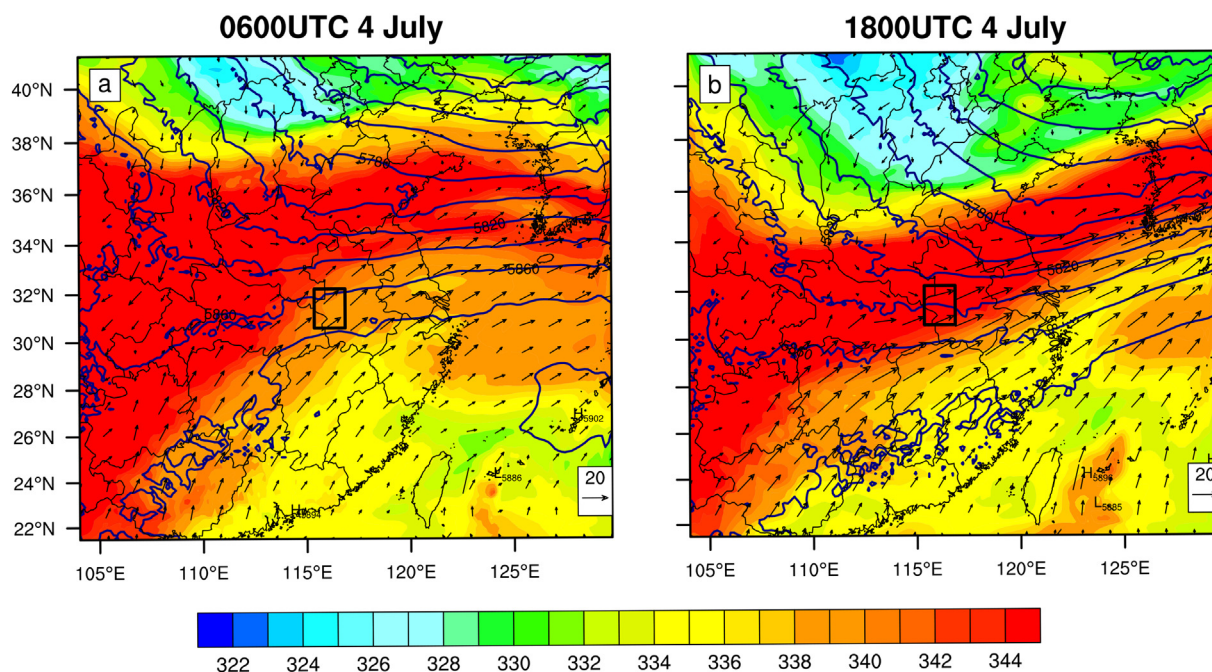


Fig. 6. As in Fig. 3, but for case0705, valid at (a) 18 h (0600UTC 4 July) and (b) 6 h (1800UTC 4 July) prior to the forecast initialized at 0000UTC 5 July. Black boxes denote the analysis area of ESA.

each ensemble within the four experiments. As shown in Fig. 8, ensembles with different experimental setups exhibit different properties. In both cases, most of the ensembles initialized by the breeding cycle show smaller RMSE than the CONTROL experiment, indicating that the bias and errors from the cycling assimilation accumulate with the model integration and degrade the forecast skill in the later stage of the forecast (beyond 24 h). The RMSE of the SENS experiments show clear trends with the change of perturbation magnitudes, for case0731, the RMSE values gradually increase first and then decrease between the magnitude of 0.125–0.75 STD, then increase again with the perturbation magnitude. For case0705, the values present a tendency of continuous decrease between 0.125 and 0.75 STD and then increase as the perturbation magnitude amplifies. In both cases the values of RMSE reach a relatively minimum value at a perturbation magnitude of 0.75 STD, although the smallest RMSE in case0731 appears at the magnitude of 0.125STD. In general, the SENS ensembles show relatively low RMSE across all perturbation magnitudes and the lowest RMSE at perturbation magnitudes of 0.25–0.75 STD.

The RMSE of the GAUSS and BGM experiments exhibits greater uncertainty across different perturbation magnitudes. For case0731, larger perturbation magnitudes in the BGM experiment lead to increased error, while the error is relatively small at magnitudes below 0.5 STD. For case0705, increasing perturbation magnitude in the BGM experiment is associated with better performance, and greater error appears at smaller magnitudes. The RMSE distribution across different magnitudes in the GAUSS experiment is relatively steady for case0731 but fluctuates for case0705. The uncertain characteristics of the GAUSS and BGM experiments indicate that the fast-growing perturbations obtained by the breeding cycle behave differently under various weather conditions. The optimal perturbation magnitude is difficult to determine. As pointed out by Hamill et al. (2000) and Wang and Bishop (2003), the simple bred method doesn't perform well in representing the case-to-case uncertainties. By contrast, the RMSE of the SENS experiment shows clear regularity with changes in perturbation magnitude, suggesting that introducing the sensitivity pattern leads to more reasonable distributions of the perturbations and systematically improves the forecasting skills. Overall, the SENS experiment exhibits better performance than that of the other two experiments. A relatively

optimal perturbation magnitude is at approximately 0.75 STD in both cases.

For an overall comparison of the precipitation forecast skill among all the ensemble experiments within the four experimental configurations, the fractions skill score (FSS) with a neighborhood size of 15 km and the threat score (TS) in the analysis box are examined for each ensemble. As shown in Fig. 9, in both cases, the SENS experiments for the various perturbation magnitudes are positioned closer to the top right corner for each precipitation threshold, which means that the FSS and the TS values in these ensembles are higher than those in the other ensembles. In addition, most of the SENS ensembles shows higher scores than the CONTROL ensemble, indicating that the SeBGM scheme achieves the purpose of correcting the bias and errors in forecasts from the cycling data assimilation system to a certain degree. Moreover, ensembles with perturbation magnitudes of 0.5 to 0.75 STD have superior performance at most rain-rate thresholds, especially for larger rain-rate thresholds in case0705. It is worth noting that although the ensemble of SENS experiment at magnitude of 0.125STD has the smallest RMSE in case0731, it shows relatively poor performance compared with the ensemble at magnitudes of 0.5–0.75STD according to the skill scores. Consistent with the inference above, the perturbation magnitudes of about 0.5–0.75STD are relatively optimal for capture the convective precipitation in this study. The performance of the BGM and GAUSS experiments varies greatly with the perturbation magnitude, rain-rate threshold and case, suggesting that the optimal perturbation magnitude of the two experiments is dependent on the meteorological conditions. Neither of them outperforms the CONTROL experiment significantly in skill scores across all the perturbation magnitudes and rain-rate thresholds. The SENS experiments adapt to the changes in weather conditions and have robust performance in different cases. In general, the SENS experiment outperforms the other three experiments across precipitation thresholds, and the advantage is more pronounced at larger thresholds ($10\text{mm} \cdot \text{h}^{-1}$).

To evaluate the impact of the additional information introduced in the SENS and GAUSS experiments, a intercomparison of the precipitation forecast skill at each perturbation magnitude is performed by calculating the Brier skill scores (BSS) and TS differences of the SENS and GAUSS experiments relative to the BGM experiment. According to

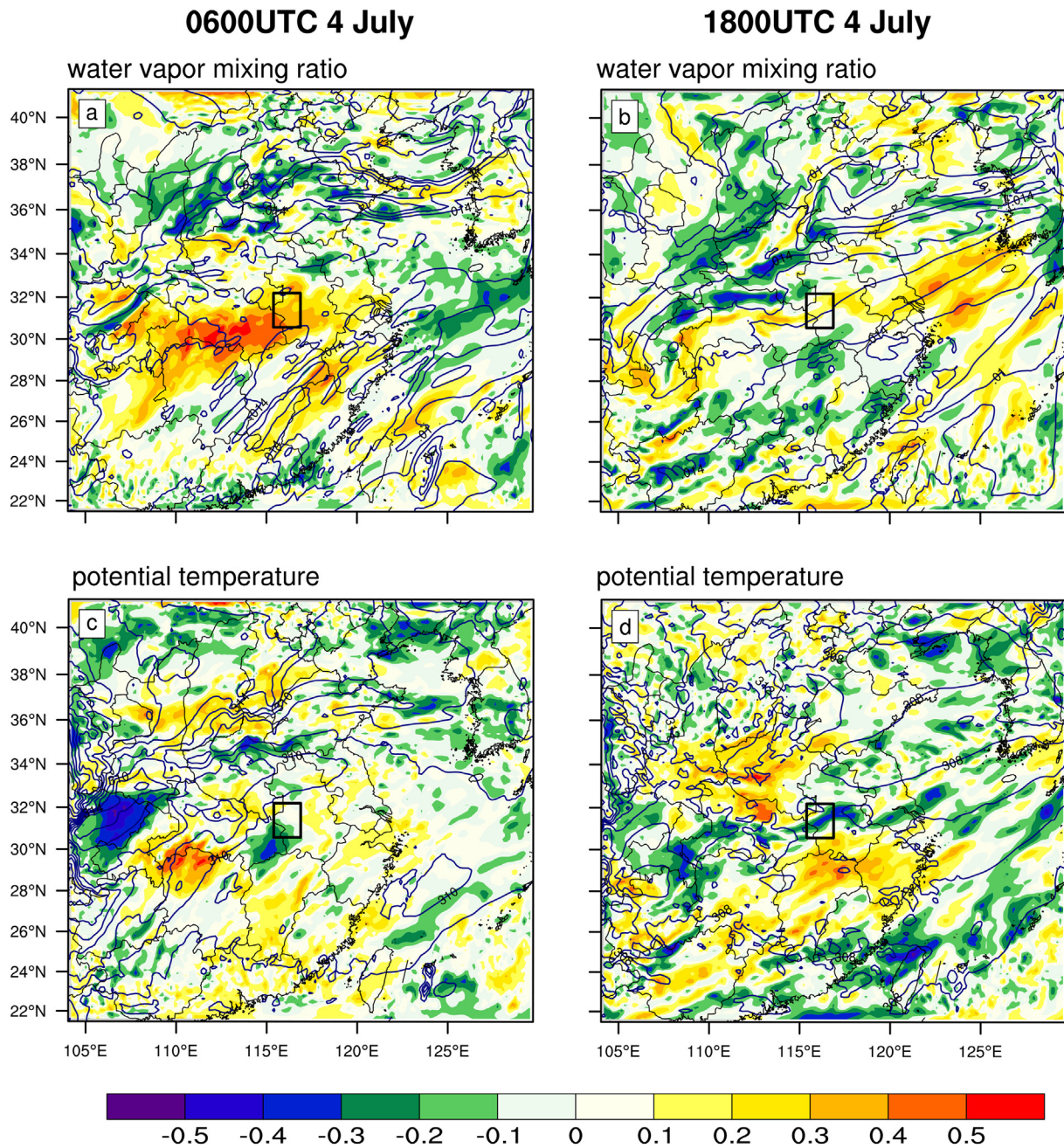


Fig. 7. Sensitivity of the spatially averaged precipitation during 2300 4 July - 0100UTC 5 July averaged over the analysis area to the 800–900 hPa water vapor mixing ratio (q_v ; a, b) and the potential temperature (θ ; c, d) for case0705, valid at (a, c) 18 h (0600UTC 4 July) and (b, d) 6 h (1800UTC 4 July) prior to the forecast initialized at 0000UTC 5 July. The contours are the ensemble mean values for $q_v(\text{kg} \cdot \text{kg}^{-1})$, a, b) and potential temperature(k , c, d). Black boxes denote the analysis area of ESA.

Fig. 10, for both cases, more SENS ensembles are located in the upper right corner quadrant across the precipitation threshold, where both the BSS and the TS values are superior to those of BGM experiments at these perturbation magnitudes. As the threshold increases, the SENS experiments show greater advantages, indicating that the introduction of the sensitivity pattern has a positive impact on the precipitation forecasts, especially at larger rain-rate thresholds. By contrast, the GAUSS experiments usually exhibit poor performance relative to the BGM experiments in at least one skill score, suggesting that there is no significant added value of introducing the Gaussian distribution into the perturbation. Similar to the previous results, the SENS experiments with perturbation magnitudes of 0.5–0.75 STD have relatively better performance at most precipitation thresholds for both cases.

Since the SENS experiment shows lower precipitation forecast error, especially at the perturbation magnitude of 0.75 STD for both cases, the forecasts of the non-precipitation variables within SENS_6, GAUSS_6 and BGM_6 experiments at this magnitude along with the CONTROL experiment are evaluated. As mentioned earlier, convection development is more sensitive to the thermodynamic conditions at low-level of atmosphere according to previous research (Hill et al., 2016; Torn and Romine, 2015; Torn et al., 2017; Berman et al., 2017). In order to explore whether the SeBGM scheme reflects such a vertical correspondence in the prediction of variables, we assess the performance of different experiments across the vertical levels. In Fig. 11, the temporally averaged RMSE and spread of the temperature, meridional wind, and specific humidity are shown for the two cases. The introduction of

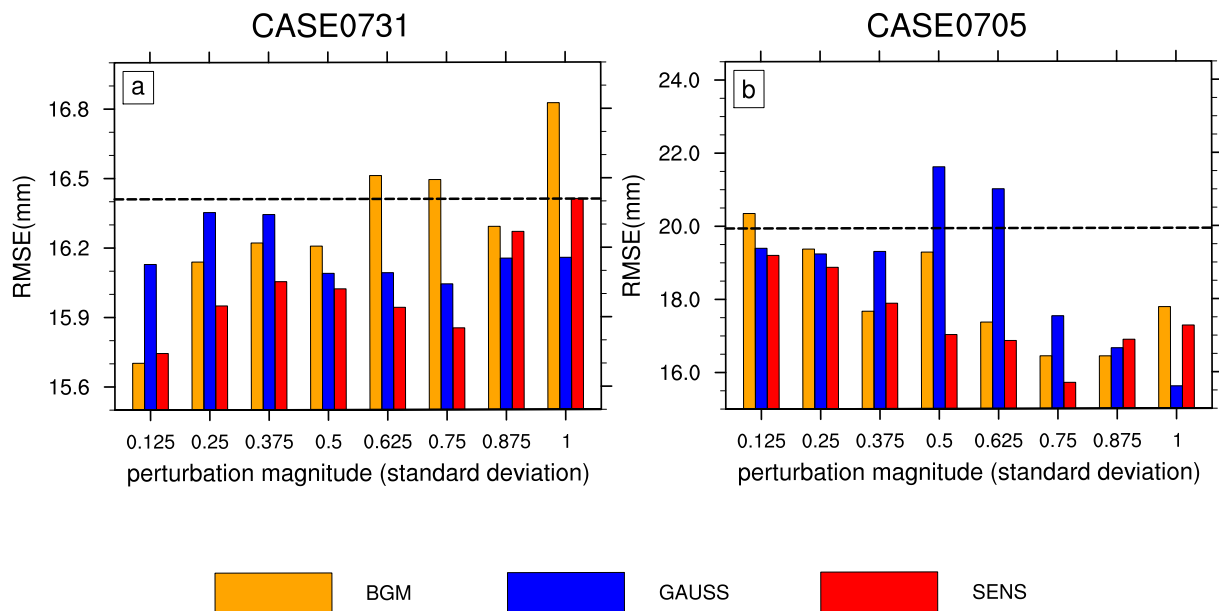


Fig. 8. The root-mean-square error (RMSE) of the ensemble mean 12 h accumulated precipitation (mm) in the analysis box from the BGM (orange), GAUSS (blue), SENS (red) at different perturbation magnitudes and the CONTROL experiment (black dash line) with respect to the observation data. The precipitation was accumulated during 0600–1800 UTC on 31 July for case0731 (a) and 0000UTC–1200UTC 5 July for case0705 (b). (For interpretation of the references to colour in this figure legend, the reader is referred to the web version of this article.)

sensitivity-based perturbations usually leads to increased spread and reduced RMSE at most levels. For case0731, the errors in temperature and moisture in the SENS₆ ensemble are reduced the most at low levels near the surface (Fig. 11a, c), whereas the error in meridional wind is reduced mostly in the middle and high levels (Fig. 11b). The spread of the SENS₆ experiment is slightly improved relative to that of the GAUSS₆ and BGM₆ experiments. The CONTROL experiment shows relatively larger spread at some levels but is accompanied by increased errors. For case0705, the reduced RMSE and enhanced spread in the SENS₆ experiment in terms of temperature and specific humidity usually appear at low and middle levels, except for the increased error in the specific humidity at 700–800 hPa (Fig. 11f). Moreover, reduction in the error of the meridional wind is also found mostly in the middle and high levels (Fig. 11e). It is worth noting that the GAUSS₆ experiment generally outperforms the BGM₆ for case0731 but performs worse than the BGM₆ for case0705, which agrees with the verification based on precipitation. The fast-growing perturbations from the breeding cycle have unstable performance in different cases, whereas the sensitivity-based perturbations are able to adapt to changes in weather conditions, producing reasonable forecasts for both precipitation and non-precipitation variables.

4.3. Impact on near-surface simulation

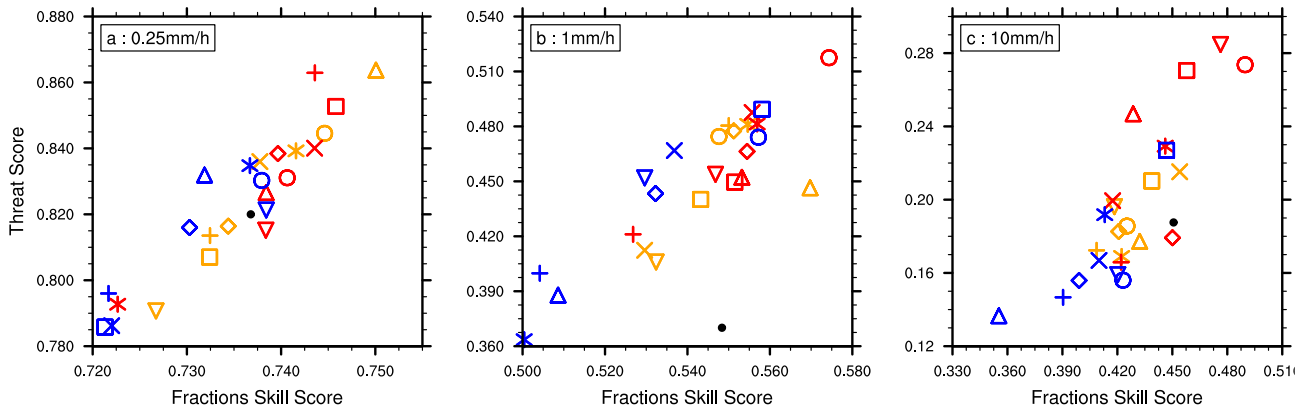
To demonstrate the impact of the introduced sensitivity patterns on the forecast in detail, the near-surface variables of the inner domain in the BGM₆ (perturbation magnitude of 0.75 STD) experiment are compared with the GAUSS₆ and SENS₆ experiments spatially and temporally in case0731. According to Fig. 12, the simulated precipitation of the BGM₆ experiment moves southeastwards and develops too fast in the early stage, whereas the strength is insufficient relative to the observation (Fig. 12d–f). The heavy precipitation in the BGM₆ experiment occurred prior to the observation but collapsed quickly, resulting in the error in the precipitation forecast in the BGM₆ experiment. The same problem lies in the GAUSS₆ experiment, but the precipitation at the back of the squall line is slightly more intensive (Fig. 12g–i). The precipitation forecast of the SENS₆ experiment is closer to the observation, especially reflected in the maintenance of

precipitation behind the squall line in the later stage (Fig. 12j–l). Since the precipitation is associated with the squall line in this case, accurate simulation of the convective system is crucial for the precipitation forecast.

Figs. 13 and 14 highlight some of the systematic differences in SENS₆ ensemble relative to the BGM₆ ensemble, which explains the mechanism of how the introduced sensitivity patterns improve the precipitation forecast. The mean state 2 m temperature from the BGM₆ ensemble at 0900UTC features a warm air mass located in the southeast of the domain and cold air in the northwest (Fig. 13a). The squall line is at the junction of the warm and cold area and moves southeast over time. The difference in the 2 m temperature between the SENS₆ and BGM₆ ensembles at 0900UTC shows a significant northeast-southwest oriented warm line near the squall line, together with strengthening of the southeast wind component in the same area (Fig. 13c). This warm line remains until 1200UTC, when the precipitation develops most intensively, and moves towards the southeast (Fig. 13d), indicating that the edge of the warm air in the SENS₆ experiment is northwest relative to that in the BGM₆. Therefore, the simulated squall line in the SENS₆ experiment moves slower towards the southeast than it does in BGM₆. In addition, the cold air behind the squall line is strengthened in the SENS₆ experiment relative to that in BGM₆ at 0900UTC, resulting in a more intensive development of the squall line in the SENS₆ experiment. By contrast, although the difference between GAUSS₆ and BGM₆ also exhibits strengthening of the cold air behind the squall line (Fig. 13e, f), it shows a relatively random distribution at 0900UTC, with no systematic difference near the squall line (Fig. 13e). At 1200UTC, the 2 m temperature near the southern part of the squall line in the GAUSS₆ ensemble shows a significant positive difference with respect to that of the BGM₆ experiment, while the area near the northern part of the squall line is significantly colder. Additionally, strengthening of the southeast and northwest wind components near the southern and northern parts of the squall line, respectively, is observed in GAUSS₆ (Fig. 13f). The differences in the analysis box remain small over time.

The mean state precipitable water of BGM₆ is concentrated mainly in the Beijing area and to the southeast, the maximum is along the position of squall line. Compared to the 2 m temperature, the gradient of precipitable water is not so strong near the squall line. Therefore the

CASE0731



CASE0705

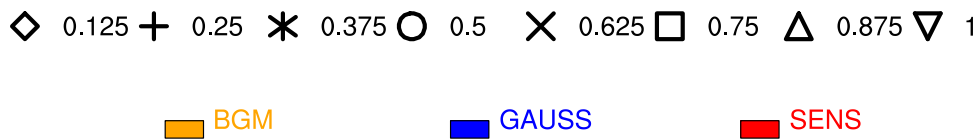
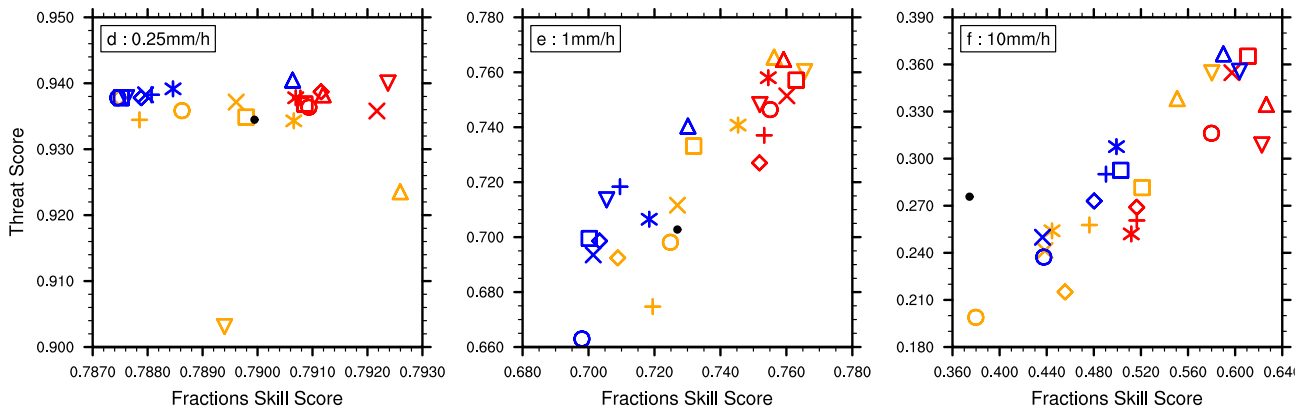


Fig. 9. Fractions skill score (FSS) with a neighborhood size of 15 km and threat score (TS) in the analysis box for case0731 (a–c) and case0705 (d–f) for BGM (orange), GAUSS (blue), SENS (red) and CONTROL (black dot) averaged over the ensemble forecasts for rain-rate thresholds of (a), (c) 0.25; (b), (d) 1.0; (e), (f) 10 $mm \cdot h^{-1}$. Each symbol denotes a perturbation magnitude in BGM, GAUSS and SENS experiments. (For interpretation of the references to colour in this figure legend, the reader is referred to the web version of this article.)

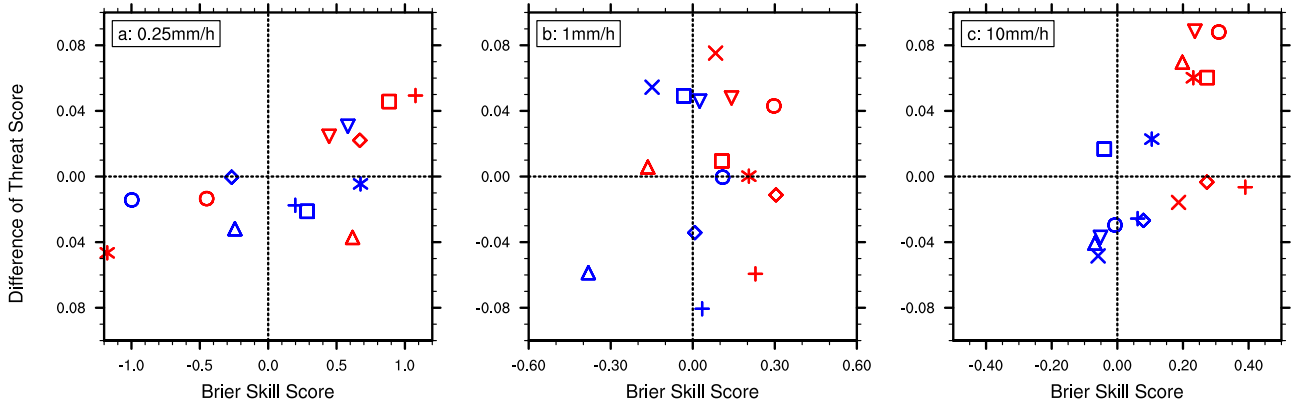
difference in the precipitable water shows less systematicness in both experiments. Despite this a long drier belt still appears in SENS₆ experiment in front of precipitable water maximum, followed by a wetter belt (Fig. 14c, d). This structure similar to a dipole signal represents a westward shift of the moisture maximum in the SENS₆ experiment. The precipitation belt of the SENS₆ experiment moves more slowly towards the southeast than it does in the BGM₆ experiment. The wetter region behind the squall line indicates the greater abundance of precipitable water in the SENS₆ experiment, leading to more intensive precipitation, which is closer to the reality. The difference between GAUSS₆ and BGM₆ shows a more random distribution near the squall line at 0900UTC (Fig. 14e). There is a significant drier region near the southwestern part of the squall line while no systematic difference is observed near the northeastern area at 1200UTC (Fig. 14f). These features demonstrate the ability of the SeBGM scheme to capture the crucial system in the forecast and to improve the simulation accuracy of the systems' movements and developments.

In addition to the difference fields, the ensemble spread of these

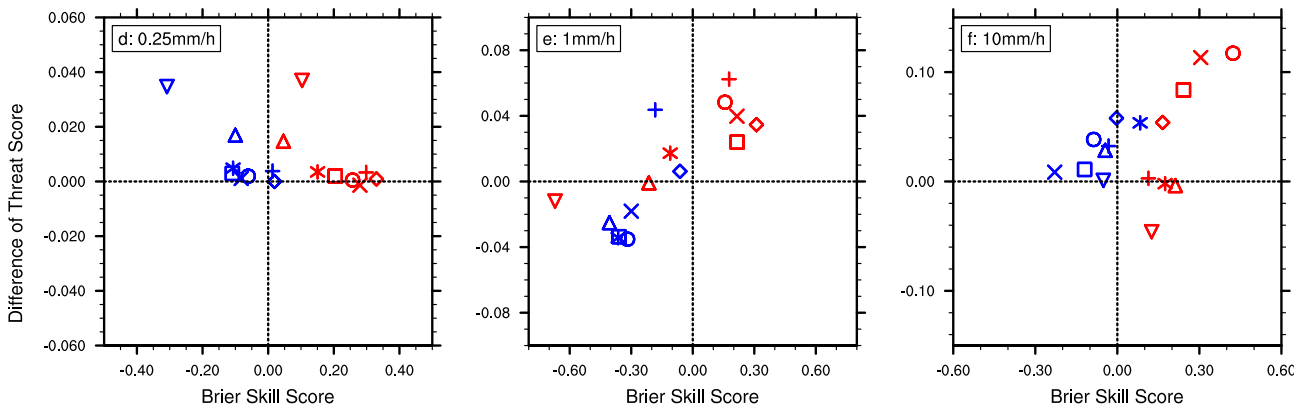
near-surface variables is also compared. As shown in Fig. 15, overall the spread difference between SENS₆ and BGM₆ experiments shows a slight increase of spread in SENS₆ experiment (Fig. 15a–c and g–i), while the GAUSS₆ experiment shows a decrease of spread (Fig. 15d–f and j–l). It is indicated that the introduced sensitivity patterns facilitate the perturbation fields to capture the uncertainty in the convection evolution, while the Gaussian distribution is not conducive to represent this uncertainty. The SENS₆ experiment shows more significant improvement of spread near the west side of the squall line at 1200UTC (Fig. 15g–i). The distribution of the spread difference is similar to the mean difference in these variables. The dipole structures also appear in spread difference fields of SENS₆ at 1200UTC, suggesting that the maximum spread in SENS₆ experiment locates more west than BGM₆.

It is noted that for all variables, the difference fields in the GAUSS₆ experiment show somehow similar characteristics to that in the SENS₆ in some areas, especially near the cold air at the back of the squall line. This may reflect some limitations of the ESA method. Since the ESA method relies on linear assumption, when the ensemble members are

CASE0731



CASE0705



◇ 0.125 + 0.25 * 0.375 ○ 0.5 × 0.625 □ 0.75 △ 0.875 ▽ 1

■ GAUSS

■ SENS

Fig. 10. Brier skill scores (BSS) with a neighborhood size of 15 km and difference of threat scores (DTS) in the analysis box for case0731 (a–c) and case0705 (d–f) for GAUSS (blue) and SENS (red) relative to BGM for the same perturbation magnitude averaged over the ensemble forecasts for rain-rate thresholds of (a), (c) 0.25; (b), (d) 1.0; (e), (f) $10 \text{ mm} \cdot \text{h}^{-1}$. Each symbol denotes a perturbation magnitude. (For interpretation of the references to colour in this figure legend, the reader is referred to the web version of this article.)

limited, the sensitivity patterns may also contain some spurious correlations and noise, thus produce effects similar to the Gaussian distribution. However, for crucial convective systems, the sensitivity patterns still provide indicative information, so that the SENS experiment has a more obvious improvement on the position forecast of the squall line.

Overall, the sensitivity-based IC perturbations provide systematic improvement in the simulation of the near-surface conditions, leading to more reasonable forecasts of convection development, such that the accuracy of the precipitation forecast is improved. These results further prove that the sensitivity relationship revealed by ESA is robust and indicative. While the sensitivity-based perturbation significantly influences the simulation of the near-surface thermodynamic features, the impact on the upper-level conditions is relatively small (not shown). This result is consistent with the RMSE values of the temperature and specific humidity, which are reduced mainly at the low levels in this case, and is also in agreement with previous studies showing that the convection forecast is more sensitive to low-level thermodynamic

features (Weisman and Rotunno, 2000; Takemi, 2007; Weisman et al., 2008; Schumacher et al., 2013; Trier et al., 2017).

5. Conclusions

This research focuses on developing and evaluating a method (SeBGM) for introducing sensitivity-based IC perturbations into CPEFs. The sensitivity of the forecast metric to the model state variable is calculated via ESA, and the sensitivity patterns at various lead times are introduced as the product of the sensitivity value and the fast-growing perturbations obtained by the breeding cycle. The effects of different amplitudes of perturbation are examined to explore the range of appropriate magnitudes for this method. The results of ensembles with a sensitivity-based perturbation scheme (SENS) are compared to those perturbed without the introduction of a sensitivity pattern (GAUSS, BGM and CONTROL). All the four experiments are initialized by the same 10 randomly selected members of the 50-member WRF-DART EAKF analysis. For SENS, GAUSS, and BGM experiments, the forecasts

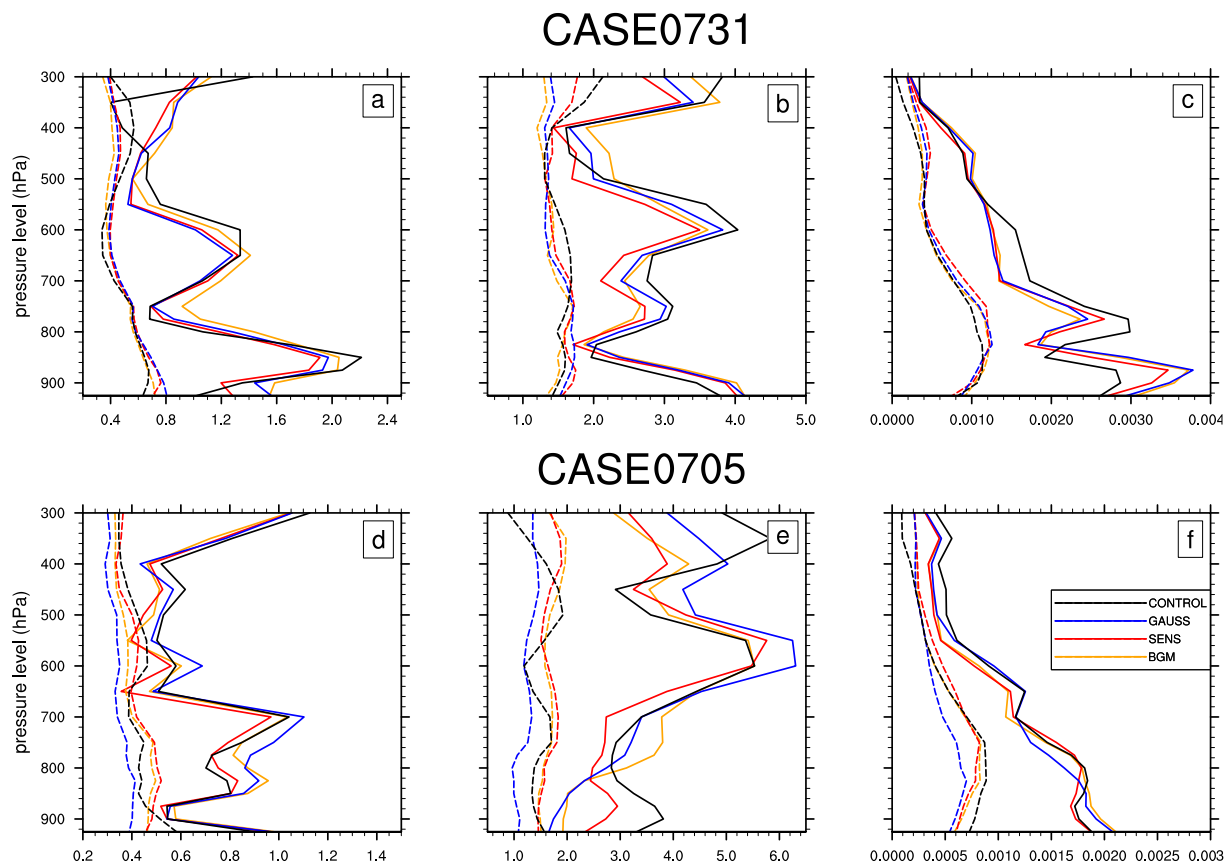


Fig. 11. The spatial and temporal averaged root-mean-square error (RMSE; solid line) and spread (dash line) of the temperature (K; a, d), v-wind component ($mm \cdot s^{-1}$; b, e) and specific humidity ($kg \cdot kg^{-1}$; c, f) for BGM_6 (orange), GAUSS_6 (blue), SENS_6 (red) at a perturbation magnitude of 0.75 STD and CONTROL (black) experiments in analysis boxes for case0731 (a–c) and case0705 (d–f). (For interpretation of the references to colour in this figure legend, the reader is referred to the web version of this article.)

are initialized after a breeding period lasting 24 h. In the GAUSS experiments, a Gaussian distribution with a mean of 0 and a standard deviation of 1 is introduced to the perturbation fields following the same procedure as that used for SENS. In the BGM experiments, no additional pattern is implemented in the breeding cycle. For CONTROL experiment, the forecast is initialized by the original analysis fields from WRF-DART without breeding period. The performances of all the four experiments (SENS, GAUSS, BGM and CONTROL) are evaluated in two convective precipitation cases.

Since sensitivity patterns represent meaningful relationships between the forecast metric (precipitation in this study) and the environment at earlier lead times, sensitivity-based perturbations exhibit reasonable and indicative development with the evolution of the weather situations. The SENS experiments show improved capability for capturing short-term convective precipitation in the analysis boxes, and the forecast skill in terms of precipitation with changes in perturbation magnitude exhibits similar trends in the two different cases. For both cases, this scheme has an optimal perturbation magnitude of approximately 0.75 STD, indicating that the sensitivity-based perturbations in this interval of amplitudes are the most suitable for representing the error evolution in the forecasts in this study. The CONTROL experiment shows relatively poor performance during the time period of comparison, which may be due to the bias and errors from the assimilation cycle accumulating with the model integration and degrade the skill in the later stage of the forecast. The performances of the other two experiments (GAUSS and BGM) are unstable at various perturbation magnitudes and in different cases. This instability may be due to the fact that the contribution of the dynamic growing error and the random error component to the forecasts is uncertain and

dependent on the weather regime. The SeBGM scheme adapts to the two different weather situations, yielding more reasonable response than do the other perturbation schemes considered in this experiment.

For both cases, the greatest improvement in the forecast skill in the SENS experiment is achieved at higher rain-rate thresholds, while the advantage of the SENS experiment is not as substantial at small thresholds. Since the precipitation forecast at larger thresholds is more sensitive to the convective system's development, the SeBGM scheme provides greater ability to represent the uncertainty related to the simulation of convective systems, as indicated by the spatial inter-comparison of three ensemble experiments in case0731. The SeBGM scheme improves the precipitation forecast by modifying the near-surface thermodynamic conditions systematically in this case, leading to a more reasonable simulation of the convective system's development and movement. The SeBGM scheme has the greatest impact on the forecast of the thermodynamic conditions at near-surface levels, and the effect is relatively weak at upper-levels, which also agrees with previous studies showing that the convection forecast is more sensitive to lower-tropospheric thermodynamic features.

This study introduced ESA-based perturbations into the ICs via relatively simple procedures to explore the feasibility of designing the sensitivity-based perturbation scheme. The method developed in this study aims to extract and utilize indicative information from the past forecast data by sensitivity analysis to improve the structure of the perturbation field. In our experiment, we set up a 50-member hindcast initialized by the EAKF cycling assimilation system to represent the historical forecast results of the past weather situations during t_0 to t_4 . In the meanwhile, to evaluate the contribution of the introduced sensitivity patterns intuitively, the observation information is not involved

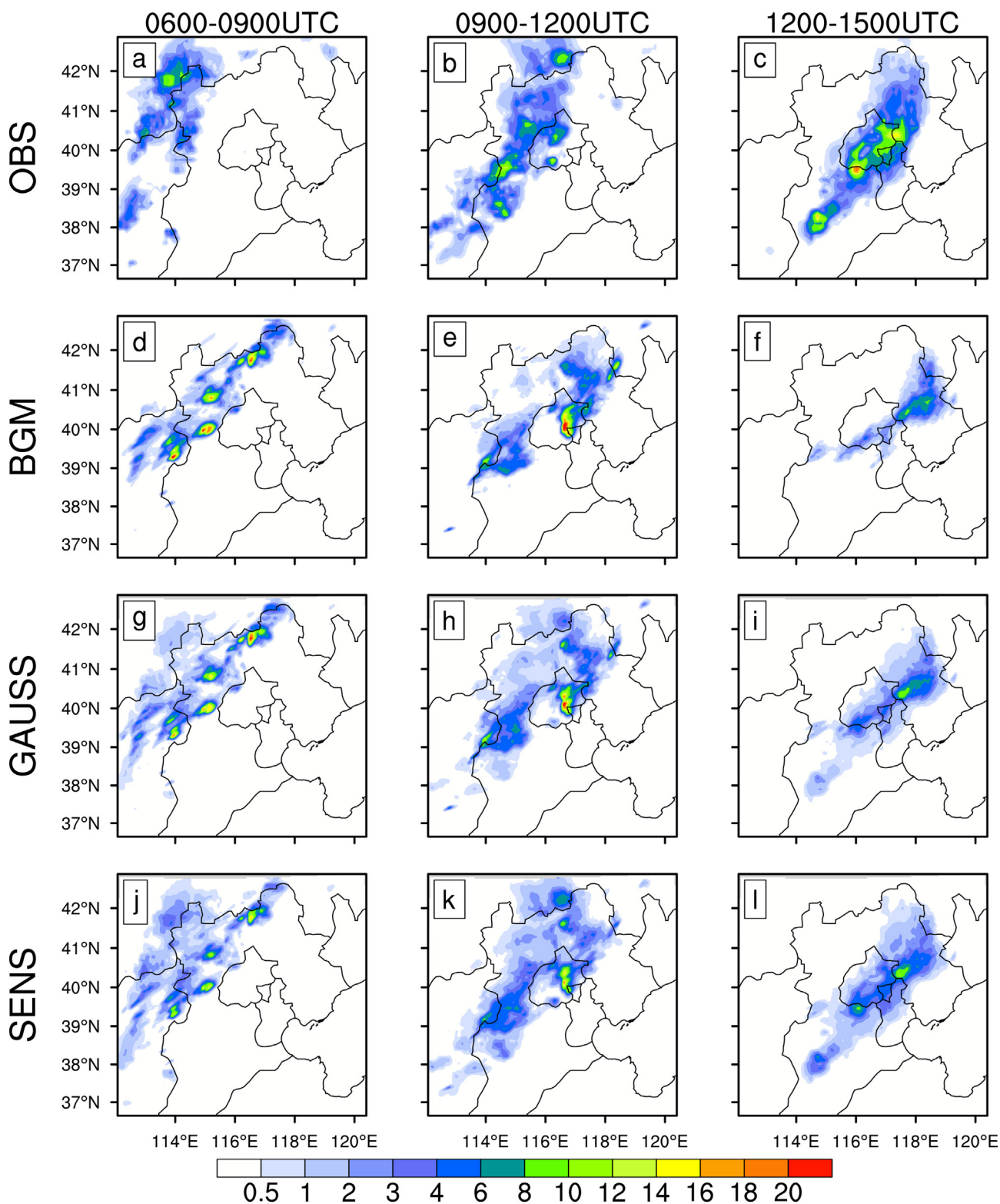


Fig. 12. Every 3 h averaged precipitation ($\text{mm} \cdot \text{h}^{-1}$) of the inner model domain in case0731 from 0600UTC to 1500UTC 31 July for the observations (a–c), BGM_6 (d–f), GAUSS_6 (g–i) and SENS_6 (j–l).

during the breeding period. In practical applications of a real-time ensemble forecast system, the method proposed in this study can improve the nowcasting of convective events according to the comparison of SENS and the other two breeding experiments (GAUSS and BGM). For a forecast initialized at t_4 , the sensitivity can be directly calculated from the historical forecast data during t_0 to t_4 . The introduction of the

sensitivity patterns can be combined with the observation data and assimilation techniques in the continuous cycle during t_0 to t_4 to improve the quality of the final analysis fields at t_4 . Besides, when comparing the SENS and CONTROL experiment, the method also shows the potential to improve the extended forecast. That is, for an ensemble forecast initialized at t_0 , the forecast in the later stage during t_4 to t_n can

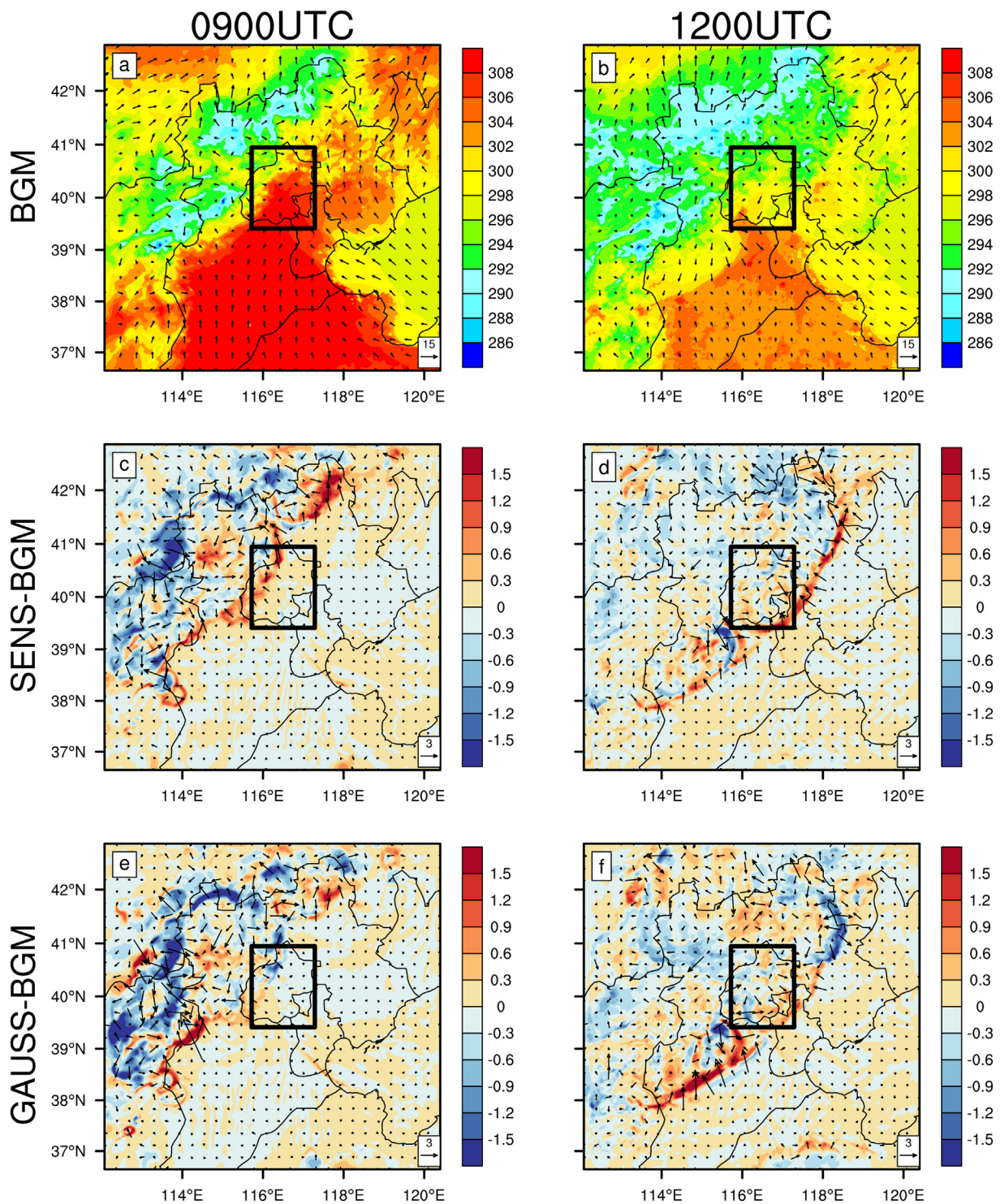


Fig. 13. Ensemble mean 2 m temperature (k) and 10 m wind vector forecast($m \cdot s^{-1}$) for the BGM_6 forecast (a–b), and mean difference from the BGM_6 for the SENS_6 (c–d) and GAUSS_6 (e–f) ensemble forecasts valid at 0900UTC (a, c, e) and 1200UTC (b, d, f) on 31 July 2013. The black boxes denote the analysis area.

be corrected by the SeBGM method, based on sensitivity analysis to the forecast in the earlier stage during t_0 to t_4 . Overall, we design this method to propose an idea that applying the sensitivity analysis to ensemble forecast at earlier lead times can extract indicative information to improve the subsequent forecast.

Although the sensitivity-based perturbation scheme indeed provides systematic improvements in the forecast of convective precipitation in this research, further implementation of this scheme should consider optimization of the parameter in the perturbation scheme, such as the

fixed analysis area and response metric, the subjectively determined perturbation magnitudes and the updating frequency of sensitivity patterns. In the meanwhile, as discussed in previous research and this study, ESA still has certain limitations in describing the development of nonlinear error, and the sampling error in the finite ensemble may cause the overestimation of the sensitivity (Wile et al., 2015; Hacker and Lei, 2015). This is an issue that needs to be specially considered in the practical application of the SeBGM method in different ensemble systems. It is necessary to combine additional technologies with the

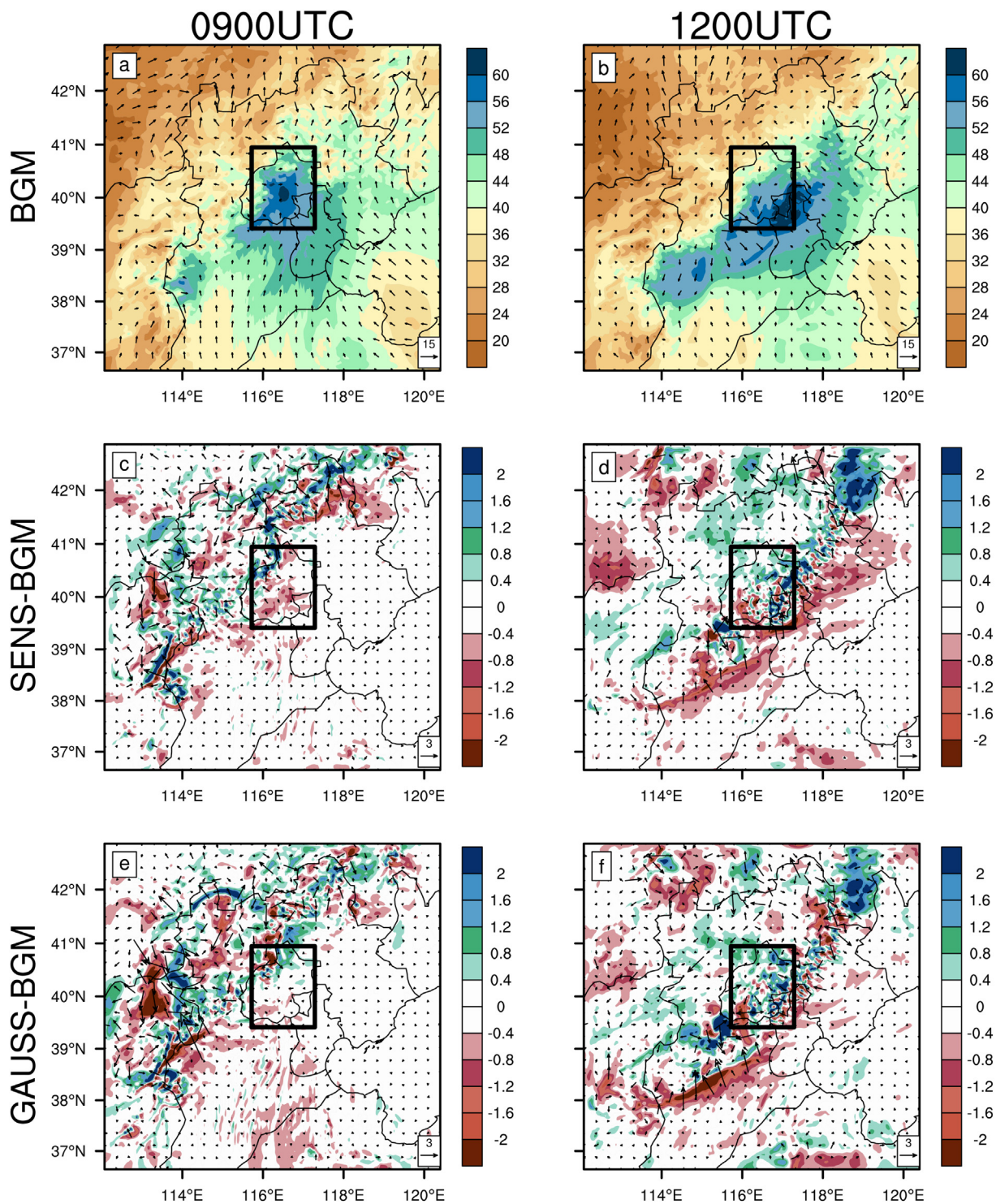


Fig. 14. As in Fig. 13, but for precipitable water (mm) and 10 m wind vectors ($m \cdot s^{-1}$).

sensitivity analysis to improve the ability to represent the uncertainty in various processes. In addition, this work demonstrates the potential of the sensitivity-based perturbation scheme in limited cases to represent different weather regimes. The robustness of the results require further investigation based on larger datasets.

Declaration of competing interest

The authors declare no conflict of interest.

Acknowledgments

This work is jointly sponsored by the National Key Research and Development Program of China (2017YFC1502103), the National Natural Science Foundation of China (41430427) and the subproject of Special Program for Key Technology Development of Operational Meteorological Forecast: Performance Evaluation of Regional Mesoscale Models for Precipitation Forecast in Qinling Mountains and Surrounding Areas [YBGJXM (2019) 05-09].

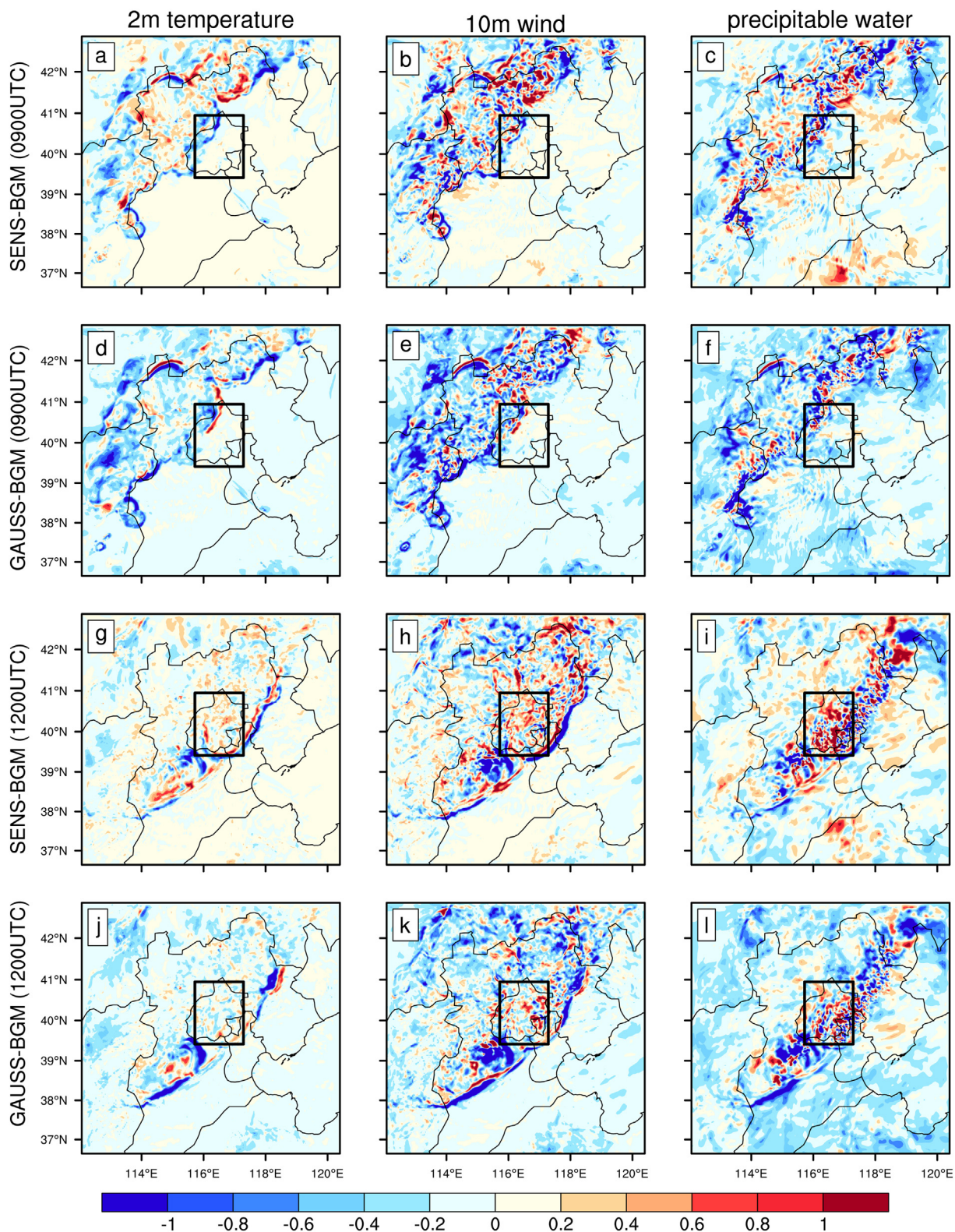


Fig. 15. The ensemble spread difference of 2 m temperature (a, c, g, j), 10 m wind speed (b, e, h, k) and precipitable water (c, f, i, l) from the BGM_6 for the SENS_6 (a–c, g–i) and GAUSS_6 (d–f, j–l) ensemble forecasts valid at 0900UTC (a–f) and 1200UTC (g–l) on 31 July 2013. The black boxes denote the analysis area.

References

Ancell, B.C., 2013. Nonlinear characteristics of ensemble perturbation evolution and their application to forecasting high-impact events. *Weather Forecast.* 28, 1353–1365. <https://doi.org/10.1175/waf-d-12-00090.1>.

Ancell, B.C., 2016. Improving high-impact forecasts through sensitivity-based ensemble subsets: demonstration and initial tests. *Weather Forecast.* 31, 1019–1036. <https://doi.org/10.1175/waf-d-15-0121.1>.

Ancell, B., Hakim, G.J., 2007. Comparing adjoint and ensemble-sensitivity analysis with applications to observation targeting. *Mon. Weather Rev.* 135, 4117–4134. <https://doi.org/10.1175/2007mwr1904.1>.

Anderson, J.L., 2001. An ensemble adjustment kalman filter for data assimilation. *Mon. Weather Rev.* 129 [https://doi.org/10.1175/1520-0493\(2001\)129](https://doi.org/10.1175/1520-0493(2001)129)

- 129 <2884:AEAKFF> 2.0.CO;2. 28842903.
- Anderson, J., 2009. Spatially and temporally varying adaptive covariance inflation for ensemble filters. *Tellus* 61A, 72–83. <https://doi.org/10.1111/j.1600-0870.2007.00361.x>.
- Barker, D., Huang, X.Y., Liu, Z., Aulign, T., Zhang, X., Rugg, S., Ajjaji, R., Bourgeois, A., Bray, J., Chen, Y., Demirtas, M., Guo, Y.R., Henderson, T., Huang, W., Lin, H.C., Michalakes, J., Rizvi, S., Zhang, X., 2012. The weather research and forecasting model's community variational/ensemble data assimilation system: Wrfda. *Bull. Am. Meteorol. Soc.* 93, 831–843. <https://doi.org/10.1175/bams-d-11-00167.1>.
- Bauer, P., Thorpe, A., Brunet, G., 2015. The quiet revolution of numerical weather prediction. *Nature* 525, 47–55. <http://www.ncbi.nlm.nih.gov/pubmed/26333465> <https://doi.org/10.1038/nature14956> Bauer, Peter Thorpe, Alan Brunet, Gilbert eng Review England 2015/09/04 06:00 Nature. 2015 Sep 3;525(7567):47-55. doi: 10.1038/nature14956.
- Bednarczyk, C.N., Ancell, B.C., 2015. Ensemble sensitivity analysis applied to a southern plains convective event. *Mon. Weather Rev.* 143, 230–249. <https://doi.org/10.1175/mwr-d-13-00321.1>.
- Berman, J.D., Torn, R.D., Romine, G.S., Weisman, M.L., 2017. Sensitivity of northern great plains convection forecasts to upstream and downstream forecast errors. *Mon. Weather Rev.* 145, 2141–2163. <https://doi.org/10.1175/mwr-d-16-0353.1>.
- Berner, J., Fossell, K.R., Ha, S.Y., Hacker, J.P., Snyder, C., 2015. Increasing the skill of probabilistic forecasts: understanding performance improvements from model-error representations. *Mon. Weather Rev.* 143, 1295–1320. <https://doi.org/10.1175/mwr-d-14-00091.1>.
- Berner, J., Achatz, U., Batt, L., Bengtsson, L., Cmara, A.d.I., Christensen, H.M., Colangeli, M., Coleman, D.R.B., Crommelin, D., Dolaptchiv, S.I., Franke, C.L.E., Friederichs, P., Imkeller, P., Jrvinen, H., Juricke, S., Kitisios, V., Lott, F., Lucarini, V., Mahajan, S., Palmer, T.N., Penland, C., Sakradzija, M., von Storch, J.S., Weisheimer, A., Weniger, M., Williams, P.D., Yano, J.I., 2017. Stochastic parameterization: toward a new view of weather and climate models. *Bull. Am. Meteorol. Soc.* 98, 565–588. <https://doi.org/10.1175/bams-d-15-00268.1>.
- Bouttier, F., Raynaud, L., Nuissier, O., Mntrier, B., 2016. Sensitivity of the arome ensemble to initial and surface perturbations during hymex. *Q. J. R. Meteorol. Soc.* 142, 390–403. <https://doi.org/10.1002/qj.2622>.
- Christensen, H.M., Moroz, I.M., Palmer, T.N., 2015. Stochastic and perturbed parameter representations of model uncertainty in convection parameterization. *J. Atmos. Sci.* 72, 2525–2544. <https://doi.org/10.1175/JAS-D-14-0250.s1>.
- Clark, P., Roberts, N., Lean, H., Ballard, S.P., Charlton-Perez, C., 2016. Convection-permitting models: a step-change in rainfall forecasting. *Meteorol. Appl.* 23, 165–181. <https://doi.org/10.1002/met.1538>.
- Deng, G., Tian, H., Li, X., Chen, J., Gong, J., Jiao, M., 2012. A comparison of breeding and ensemble transform vectors for global ensemble generation. *Acta Meteorol. Sin.* 26, 52–61. <https://doi.org/10.1007/s13351-012-0105-4>.
- Duda, J.D., Gallus, W.A., 2013. The impact of large-scale forcing on skill of simulated convective initiation and upscale evolution with convection-allowing grid spacings in the wrf*. *Weather Forecast.* 28, 994–1018. <https://doi.org/10.1175/waf-d-13-00005.1>.
- Dudhia, J., 1989. Numerical study of convection observed during the winter monsoon experiment using a mesoscale twodimensional model. *J. Atmos. Sci.* 46, 3077–3107. [https://doi.org/10.1175/1520-0469\(1989\)046<3077:NSOCOD>2.0.CO;2](https://doi.org/10.1175/1520-0469(1989)046<3077:NSOCOD>2.0.CO;2).
- Ek, M.B., 2003. Implementation of noah land surface model advances in the national centers for environmental prediction operational mesoscale eta model. *J. Geophys. Res.* 108. <https://doi.org/10.1029/2002jd003296>.
- Errico, R.M., Vukicevic, T., 1992. Sensitivity analysis using an adjoint of the psu-near mesoscale model. *Mon. Weather Rev.* 120. [https://doi.org/10.1175/1520-0493\(1992\)120<1644:SAUAAO>2.0.CO;2](https://doi.org/10.1175/1520-0493(1992)120<1644:SAUAAO>2.0.CO;2). 16441660.
- Errico, R.M., Raeder, K.D., Fillion, L., 2016. Examination of the sensitivity of forecast precipitation rates to possible perturbations of initial conditions. *Tellus A: Dyn. Meteorol. Oceanogr.* 55, 88–105. <https://doi.org/10.3402/tellusa.v55i1.12083>.
- Gao, Y., Leung, L.R., Zhao, C., Hagos, S., 2017. Sensitivity of us summer precipitation to model resolution and convective parameterizations across gray zone resolutions. *J. Geophys. Res.-Atmos.* 122, 2714–2733. URL: < Go to ISI > :// WOS:000398064200012. <https://doi.org/10.1002/2016jd025896>.
- Garcia-Ortega, E., Lopez, L., Sanchez, J.L., 2009. Diagnosis and sensitivity study of two severe storm events in the southeastern andes. *Atmos. Res.* 93, 161–178. URL: < Go to ISI > :// WOS:000267743900017. <https://doi.org/10.1016/j.atmosres.2008.10.030>.
- Gebhardt, C., Theis, S.E., Paulat, M., Ben Bouallgue, Z., 2011. Uncertainties in cosmo-de precipitation forecasts introduced by model perturbations and variation of lateral boundaries. *Atmos. Res.* 100, 168–177. <https://doi.org/10.1016/j.atmosres.2010.12.008>.
- Greybush, S.J., Saslo, S., Grumm, R., 2017. Assessing the ensemble predictability of precipitation forecasts for the January 2015 and 2016 east coast winter storms. *Weather Forecast.* 32, 1057–1078. <https://doi.org/10.1175/waf-d-16-0153.1>.
- Hacker, J.P., Lei, L., 2015. Multivariate ensemble sensitivity with localization. *Mon. Weather Rev.* 143, 20132027. <https://doi.org/10.1175/MWR-D-14-00309.1>.
- Hamill, T.M., Snyder, C., Morss, R.E., 2000. A comparison of probabilistic forecasts from bred, singular-vector, and perturbed observation ensembles. *Mon. Weather Rev.* 128, 1835–1851. [https://doi.org/10.1175/1520-0493\(2000\)128<1835:acopff>2.0.CO;2](https://doi.org/10.1175/1520-0493(2000)128<1835:acopff>2.0.CO;2).
- Hanley, K.E., Kirshbaum, D.J., Roberts, N.M., Leoncini, G., 2013. Sensitivities of a squall line over central europe in a convective-scale ensemble. *Mon. Weather Rev.* 141, 112–133. <https://doi.org/10.1175/mwr-d-12-00013.1>.
- Hill, A.J., Weiss, C.C., Ancell, B.C., 2016. Ensemble sensitivity analysis for mesoscale forecasts of dryline convection initiation. *Mon. Weather Rev.* 144, 4161–4182. <https://doi.org/10.1175/mwr-d-15-0338.1>.
- Hitchcock, S.M., Coniglio, M.C., Knopfmeier, K.H., 2016. Impact of mpex upsonde observations on ensemble analyses and forecasts of the 31 may 2013 convective event over Oklahoma. *Mon. Weather Rev.* 144, 2889–2913. <https://doi.org/10.1175/mwr-d-15-0344.1>.
- Hohenegger, C., Schär, C., 2007. Predictability and error growth dynamics in cloud-resolving models. *J. Atmos. Sci.* 64, 4467–4478. <https://doi.org/10.1175/2007jas2143.1>.
- Hong, S.Y., Noh, Y., Dudhia, J., 2006. A new vertical diffusion package with an explicit treatment of entrainment processes. *Mon. Weather Rev.* 134, 2318–2341. <https://doi.org/10.1175/MWR3199.1>.
- Kain, J.S., 2003. The kainfrisch convective parameterization: an update. *J. Appl. Meteorol.* 43, 170–181. [https://doi.org/10.1175/1520-0450\(2004\)043<0170:TKCPAU>2.0.CO;2](https://doi.org/10.1175/1520-0450(2004)043<0170:TKCPAU>2.0.CO;2).
- Kain, J.S., Weiss, S.J., Levit, J.J., Baldwin, M.E., Bright, D.R., 2006. Examination of convection-allowing configurations of the wrf model for the prediction of severe convective weather: the spc/nssl spring program 2004. *Weather Forecast.* 21, 167–181. URL: < Go to ISI > :// WOS:000237194800003. <https://doi.org/10.1175/waf906.1> times Cited: 101 1 104.
- Kain, J.S., Coniglio, M.C., Correia, J., Clark, A.J., Marsh, P.T., Ziegler, C.L., Lakshmanan, V., Stuart Jr., D.M., Dembek, S.R., Weiss, S.J., Kong, F., Xue, M., Sobash, R.A., Dean, A.R., Jirak, I.L., Melick, C.J., 2013. A feasibility study for probabilistic convection initiation forecasts based on explicit numerical guidance. *Bull. Am. Meteorol. Soc.* 94, 1213–1225. <https://doi.org/10.1175/bams-d-11-00264.1>.
- Li, J., Du, J., Zhang, D.L., Cui, C., Liao, Y., 2014. Ensemble-based analysis and sensitivity of mesoscale forecasts of a vortex over Southwest China. *Q. J. R. Meteorol. Soc.* 140, 766–782. <https://doi.org/10.1002/qj.2200>.
- Limpert, G.L., Houston, A.L., 2018. Ensemble sensitivity analysis for targeted observations of supercell thunderstorms. *Mon. Weather Rev.* 146, 1705–1721. <https://doi.org/10.1175/mwr-d-17-0029.1>.
- Lorenz, E.N., 1969. The predictability of a flow which possesses many scales of motion. *Tellus* 21, 289–307. <https://doi.org/10.3402/tellusa.v21i3.10086>.
- Martin, W.J., Xue, M., 2006. Sensitivity analysis of convection of the 24 may 2002 ihop case using very large ensembles. *Mon. Weather Rev.* 134, 192207. <https://doi.org/10.1175/MWR3061.1>.
- Melhauser, C., Zhang, F., 2012. Practical and intrinsic predictability of severe and convective weather at the mesoscales. *J. Atmos. Sci.* 69, 3350–3371. <https://doi.org/10.1175/jas-d-11-0315.1>.
- Mlawer, E.J., Taubman, S.J., Brown, P.D., Iacono, M.J., Clough, S.A., 1997. Radiative transfer for inhomogeneous atmospheres: Rrtm, a validated correlated-k model for the longwave. *J. Geophys. Res. Atmos.* 102, 16663–16682. <https://doi.org/10.1029/97jd00237>.
- Mulena, G.C., Allende, D.G., Puliafito, S.E., Lakkis, S.G., Cremades, P.G., Ulke, A.G., 2016. Examining the influence of meteorological simulations forced by different initial and boundary conditions in volcanic ash dispersion modelling. *Atmos. Res.* 176, 29–42. URL: < Go to ISI > :// WOS:000374625100004. <https://doi.org/10.1016/j.atmosres.2016.02.009> times Cited: 101.
- Peralta, C., Ben Bouallgue, Z., Theis, S.E., Gebhardt, C., Buchhold, M., 2012. Accounting for initial condition uncertainties in cosmo - de - eps. *J. Geophys. Res. Atmos.* 117. <https://doi.org/10.1029/2011jd016581>. n/a-n/a.
- Roberts, N.M., Lean, H.W., 2008. Scale-selective verification of rainfall accumulations from high-resolution forecasts of convective events. *Mon. Weather Rev.* 136, 78–97. <https://doi.org/10.1175/2007mwr2123.1>.
- Romine, G.S., Schwartz, C.S., Snyder, C., Anderson, J.L., Weisman, M.L., 2013. Model bias in a continuously cycled assimilation system and its influence on convection-permitting forecasts. *Mon. Weather Rev.* 141, 1263–1284. URL: < Go to ISI > :// WOS:000316991900006. <https://doi.org/10.1175/mwr-d-12-00112.1> times Cited: 42 0 42.
- Rotach, M.W., Ambrosetti, P., Ament, F., Appenzeller, C., Arpagaus, M., Bauer, H.S., Behrendt, A., Bouttier, F., Buzzi, A., Corazza, M., Davolio, S., Denhard, M., Dorninger, M., Fontannaz, L., Frick, J., Fundel, F., Germann, U., Gorgas, T., Hegg, C., Hering, A., Keil, C., Liniger, M.A., Marsigli, C., McTaggart-Cowan, R., Montaini, A., Mylne, K., Ranzi, R., Richard, E., Rossa, A., Santos-Muoz, D., Schr, C., Seity, Y., Staudinger, M., Stoll, M., Volkert, H., Walsler, A., Wang, Y., Werhahn, J., Wulfmeyer, V., Zappa, M., 2009. Map d-phase: real-time demonstration of weather forecast quality in the alpine region. *Bull. Am. Meteorol. Soc.* 90, 1321–1336. <https://doi.org/10.1175/2009bams2776.1>.
- Schumacher, R.S., Clark, A.J., Xue, M., Kong, F., 2013. Factors influencing the development and maintenance of nocturnal heavy-rain-producing convective systems in a storm-scale ensemble. *Mon. Weather Rev.* 141, 2778–2801. <https://doi.org/10.1175/mwr-d-12-00239.1>.
- Schwartz, C.S., Sobash, R.A., 2017. Generating probabilistic forecasts from convection-allowing ensembles using neighborhood approaches: a review and recommendations. *Mon. Weather Rev.* 145, 3397–3418. <https://doi.org/10.1175/MWR-D-16-0400.1>.
- Schwartz, C.S., Romine, G.S., Sobash, R.A., Fossell, K.R., Weisman, M.L., 2015. Nears experimental real-time convection-allowing ensemble prediction system. *Weather Forecast.* 30, 1645–1654. <https://doi.org/10.1175/waf-d-15-0103.1>.
- Seity, Y., Brousseau, P., Malardel, S., Hello, G., Bnard, P., Bout-tier, F., Lac, C., Masson, V., 2011. The arome-france convective-scale operational model. *Mon. Weather Rev.* 139, 976–991. <https://doi.org/10.1175/2010mwr3425.1>.
- Shutts, G., Pallares, A.C., 2014. Assessing parametrization uncertainty associated with horizontal resolution in numerical weather prediction models. *Philos. Trans. A Math. Phys. Eng. Sci.* 372, 20130284. <http://www.ncbi.nlm.nih.gov/pubmed/24842034>. <https://doi.org/10.1098/rsta.2013.0284>.
- Surcel, M., Zawadzki, I., Yau, M.K., 2016. The case-to-case variability of the predictability of precipitation by a storm-scale ensemble forecasting system. *Mon. Weather Rev.* 144, 193–212. <https://doi.org/10.1175/mwr-d-15-0232.1>.
- Surcel, M., Zawadzki, I., Yau, M.K., Xue, M., Kong, F., 2017. More on the scale

- dependence of the predictability of precipitation patterns: extension to the 200913 caps spring experiment ensemble forecasts. *Mon. Weather Rev.* 145, 3625–3646. <https://doi.org/10.1175/mwr-d-16-0362.1>.
- Takemi, T., 2007. A sensitivity of squall-line intensity to environmental static stability under various shear and moisture conditions. *Atmos. Res.* 84, 374–389. URL: <Go to ISI>://WOS:000247157000009. <https://doi.org/10.1016/j.atmosres.2006.10.001> times Cited: 20 Takemi, Tetsuya/0000-0002-7596-2373 0 22.
- Thompson, G., Field, P.R., Rasmussen, R.M., Hall, W.D., 2008. Explicit forecasts of winter precipitation using an improved bulk microphysics scheme. Part ii: implementation of a new snow parameterization. *Mon. Weather Rev.* 136, 5095–5115. <https://doi.org/10.1175/2008mwr2387.1>.
- Torn, R.D., Hakim, G.J., 2008. Ensemble-based sensitivity analysis. *Mon. Weather Rev.* 136, 663–677. <https://doi.org/10.1175/2007mwr2132.1>.
- Torn, R.D., Romine, G.S., 2015. Sensitivity of Central Oklahoma convection forecasts to upstream potential vorticity anomalies during two strongly forced cases during mpex. *Mon. Weather Rev.* 143, 4064–4087. <https://doi.org/10.1175/mwr-d-15-0085.1>.
- Torn, R.D., Romine, G.S., Galarneau, T.J., 2017. Sensitivity of dryline convection forecasts to upstream forecast errors for two weakly forced mpex cases. *Mon. Weather Rev.* 145, 1831–1852. <https://doi.org/10.1175/mwr-d-16-0457.1>.
- Toth, Z., Kalnay, E., 1993. Ensemble forecasting at nmc: the generation of perturbation. *Bull. Am. Meteorol. Soc.* 74, 23172330. [https://doi.org/10.1175/1520-0477\(1993\)074<2317:EFANTG>2.0.CO;2](https://doi.org/10.1175/1520-0477(1993)074<2317:EFANTG>2.0.CO;2).
- Toth, Z., Kalnay, E., 1997. Ensemble forecasting at ncep and the breeding method. *Mon. Weather Rev.* 125, 32973319. [https://doi.org/10.1175/1520-0493\(1997\)125<3297:EFANAT>2.0.CO;2](https://doi.org/10.1175/1520-0493(1997)125<3297:EFANAT>2.0.CO;2).
- Trier, S.B., Wilson, J.W., Ahijevych, D.A., Sobash, R.A., 2017. Mesoscale vertical motions near nocturnal convection initiation in pecan. *Mon. Weather Rev.* 145, 2919–2941. <https://doi.org/10.1175/mwr-d-17-0005.1>.
- Wang, X., Bishop, C.H., 2003. A comparison of breeding and ensemble transform kalman filter ensemble forecast schemes. *J. Atmos. Sci.* 60, 1140–1158. [https://doi.org/10.1175/1520-0469\(2003\)060<1140:ACOBAE>2.0.CO;2](https://doi.org/10.1175/1520-0469(2003)060<1140:ACOBAE>2.0.CO;2).
- Wang, B., Tan, X., 2010. Conditional nonlinear optimal perturbations: adjoint-free calculation method and preliminary test. *Mon. Weather Rev.* 138, 1043–1049. <https://doi.org/10.1175/2009mwr3022.1>.
- Weisman, M.L., Rotunno, R., 2000. The use of vertical wind shear versus helicity in interpreting supercell dynamics. *J. Atmos. Sci.* 57, 1452–1472. [https://doi.org/10.1175/1520-0469\(2000\)057<1452:TUOVWS>2.0.CO;2](https://doi.org/10.1175/1520-0469(2000)057<1452:TUOVWS>2.0.CO;2).
- Weisman, M.L., Davis, C., Wang, W., Manning, K.W., Klemp, J.B., 2008. Experiences with 036-h explicit convective forecasts with the wrf-arw model. *Weather Forecast.* 23, 407–437. <https://doi.org/10.1175/2007waf2007005.1>.
- Wile, S.M., Hacker, J.P., Chilcoat, K.H., 2015. The potential utility of highresolution ensemble sensitivity analysis for observation placement during weak flow in complex terrain. *Weather Forecast.* 30, 1521–1536. <https://doi.org/10.1175/waf-d-14-00066.1>.
- Xie, P., Xiong, A.Y., 2011. A conceptual model for constructing highresolution gauge-satellite merged precipitation analyses. *J. Geophys. Res. Atmos.* 116. <https://doi.org/10.1029/2011jd016118>.
- Xie, B., Zhang, F., Zhang, Q., Poterjoy, J., Weng, Y., 2013. Observing strategy and observation targeting for tropical cyclones using ensemble-based sensitivity analysis and data assimilation. *Mon. Weather Rev.* 141, 1437–1453. <https://doi.org/10.1175/mwr-d-12-00188.1>.
- Yokota, S., Seko, H., Kunii, M., Yamauchi, H., Niino, H., 2016. The tornadic supercell on the kanto plain on 6 may 2012: polarimetric radar and surface data assimilation with enfk and ensemble-based sensitivity analysis. *Mon. Weather Rev.* 144, 3133–3157. <https://doi.org/10.1175/mwr-d-15-0365.1>.
- Zacharov, P., Rezacova, D., 2009. Using the fractions skill score to assess the relationship between an ensemble qpf spread and skill. *Atmos. Res.* 94, 684–693. <https://doi.org/10.1016/j.atmosres.2009.03.004>.
- Zhang, H., Pu, Z., 2010. Beating the uncertainties: ensemble forecasting and ensemble-based data assimilation in modern numerical weather prediction. *Adv. Meteorol.* 2010, 1–10. <https://doi.org/10.1155/2010/432160>.